

University of Alberta

**Inhaled Aerosols Targeted via Magnetic Alignment of High Aspect Ratio
Particles: An In Vivo and Optimization Study**

by

Gillian Elizabeth Scholey Redman

A thesis submitted to the Faculty of Graduate Studies and Research
in partial fulfillment of the requirements for the degree of

Master of Science

Department of Mechanical Engineering

© Gillian Elizabeth Scholey Redman

Spring 2011

Edmonton, Alberta

Permission is hereby granted to the University of Alberta Libraries to reproduce single copies of this thesis and to lend or sell such copies for private, scholarly or scientific research purposes only. Where the thesis is converted to, or otherwise made available in digital form, the University of Alberta will advise potential users of the thesis of these terms.

The author reserves all other publication and other rights in association with the copyright in the thesis and, except as herein before provided, neither the thesis nor any substantial portion thereof may be printed or otherwise reproduced in any material form whatsoever without the author's prior written permission.

Abstract

An *in vivo* study with 19 rabbits was completed. Half of the exposed rabbits had a magnetic field placed externally over their right lung. Magnetic resonance images of the lungs were acquired to determine the iron concentrations in the right and left lung of each animal. The right/left ratio increased in the middle and basal regions of the lung. With further optimization, this technique could be an effective method for targeted drug delivery.

Additionally, the feasibility of increasing the length of high aspect ratio particles for improved targeted drug delivery was explored. An ultrasonic nozzle was pulsed into a large evaporation chamber. Individual particles were found to be double the original length. However, due to locally increased humidity the droplets were not dried, except with the use of an orifice to rapidly accelerate and break apart the larger droplets. The complications associated with this method make it an undesirable and unfeasible method of creating longer particles.

Acknowledgements

Firstly, I would like to thank Dr Warren Finlay for his support throughout the past two years. Without his insight and guidance this research would not have been possible. I would also like to thank Helena Orszanka for preparing an endless number of samples, preparing an incredible number of microscope samples, and answering every last question I had about cromoglycic acid. I would also like to thank all the ARLA researchers for making coming into work every day a joy, but mostly for subsidizing my coffee addiction through a clever scheme called the “coffee club”.

I would also like to thank all the researchers who contributed to the *in vivo* study. Andrew Martin, who originally designed the experimental set-up and answered endless questions via email, Paul Waszak who performed the surgical components of the study, Richard Thompson who performed all the MRI analysis, and Bernard Thébaud and Po-Yin Chen who generously donated lab space.

I would also like to thank Dr Ming Chen for performing all the SEM analysis and patiently searching for tiny particles.

On a personal note, I'd like to thank all the wonderful friends I've made here at the University, who not only made Edmonton feel like home but made it a difficult place to leave. Having left Alberta and moved east, Marc Schostek and Aaron Baugh can once again be Western Canada's prettiest and second prettiest fluid dynamicists (the order is at your discretion). I'd finally like to thank my family for all their support and my boyfriend Ryan for giving me the motivation I needed to finish.

For their financial support I'd like to thank the Department of Mechanical Engineering and Queen Elizabeth II scholarship.

Table of Contents

1	Introduction	1
1.1	Inhaled Pharmaceutical Aerosols.....	1
1.2	Lung Cancer and Inhaled Chemotherapy.....	1
1.3	Summary of Thesis.....	2
2	Background	4
2.1	Characteristics of the Respiratory Tract	4
2.2	Aerosol Deposition in the Lung.....	7
2.2.1	Aerosol Particle Motion	7
2.2.2	Mechanisms of Deposition	8
2.2.3	Deposition of HARPs	9
2.3	Applications of pharmaceutical aerosols.....	10
2.4	Targeted aerosol drug delivery.....	12
2.4.1	Previous work.....	12
2.4.2	Magnetic Targeting with HARPs	14
3	Pilot study of inhaled aerosols targeted via magnetic alignment of HARPs in rabbits	17
3.1	Introduction	17
3.2	Methods.....	17
3.2.1	Aerosol Production	17
3.2.2	Animals.....	20
3.2.3	Exposure.....	20
3.2.4	Measurement of Deposition	23
3.3	Results.....	30
3.4	Discussion.....	32
3.5	Conclusion.....	36
4	Feasibility of optimizing HARP length for targeted drug delivery	38
4.1	Introduction	38
4.2	Experimental Methods	41
4.2.1	Preparation of Ultrasonic Nozzle Suspensions	41

4.2.2	Aerosol Generation	41
4.2.3	Drying of droplets	44
4.2.4	Orifice Design	55
4.2.5	Sample Collection and Imaging.....	58
4.3	Results and Discussion	62
4.3.1	Expected particle morphology	62
4.3.2	Interpretation of SEM images to infer 3D particle morphology	64
4.3.3	Sizing of individual CA HARPs.....	70
4.3.4	Ultrasonic nozzle aerosol particle collection and imaging.....	72
4.4	Conclusions	90
5	Suggestions for Future Work	91
	References	92

List of Tables

Table 1: Airway diameters and lengths for each generation from Finlay et al [18]	6
Table 2: Regional and total area-averaged T_1 relaxation times and iron concentrations for the left and right lung of non-targeted and targeted rabbits	31
Table 3: Evaporation chamber residence times for a 50 micron droplet for flow rates of 18, 11, and 0.2 l/min	52
Table 4: Results for integral and Kolmogorov turbulence scales for orifice	57
Table 5: Experimental settings for sizing experiment.....	58
Table 6: Experimental settings for ultrasonic nozzle generated HARPs	62
Table 7: Sizing parameters for individual CA particles created	72
Table 8: Comparison of predicted and actual particle concentrations in areas A and B..	84

List of Figures

Figure 1: Alignment of HARPs in the lung (a) naturally (b) in the presence of a magnetic field	15
Figure 2: SEM image of high aspect ratio particles (HARPs) of CA and FeREX. The light coloured aligned particles are the HARPs and the small black dots are the pores of the membrane.....	19
Figure 3: Schematic of mechanical ventilation circuit used to expose rabbits to aerosol. ETT = endotracheal tube.....	21
Figure 4: Location of rabbit relative to permanent magnets used to generate magnetic field	22
Figure 5: Nonlinear regression fit to SI curve	25
Figure 6: MRI images at various T_i times: (a) 100 ms (b) 300 ms (c) 600 ms (d) 1000 ms (e) 1500 ms (f) 2000 ms (g) 3000 ms (h) 4000 ms	26
Figure 7: MRI images at $T_i = 4000$ ms spanning from the apex to the diaphragm	27
Figure 8: Sample of image processing: (a) original MRI image (b) after selection of region of interest (c) after removal of vasculature (d) iron concentrations in $\mu\text{g}/\text{cm}^3$	29
Figure 9: Aerodynamic diameter (d_{ae}) size distributions weighted by mass of iron and mass of cromoglycic acid, as determined by cascade impaction for the iron oxide loaded cromoglycic acid aerosol. Asterisks indicate statistically significant differences between the two distributions ($P < 0.05$; two-tailed student's t-test for independent samples)...	30
Figure 10: Ratios of regional right to left lung iron concentrations in targeted and non-targeted rabbits. Error bars represent standard errors of the mean	32
Figure 11: Ratios of iron concentration between middle and apical, and basal and apical regions of the left and right lungs of targeted and non-targeted rabbits. Error bars represent standard errors of the mean	32
Figure 12: Deposition probabilities for HARPs of varying length and diameter in an airway bifurcation representing the branching between lung generations 14 and 15....	39
Figure 13: Droplet diameters for various ultrasonic nozzle operating frequencies (Sonotek, Milton, NY, USA)	43
Figure 14: Schematic of Ultrasonic Nozzle System	44
Figure 15: Settling velocities calculated for water droplets with diameters from 1 to 100 microns	45
Figure 16: Droplet lifetimes for water droplets with diameters ranging from 1 to 100 microns for relative humidities of 0% and 35%.....	48
Figure 17: Droplet lifetimes for a 50 micron droplet of water at relative humilities ranging from 0% to 100%.....	49

Figure 18: Experimental set-up of ultrasonic nozzle with evaporation chamber schematic	51
Figure 19: Final evaporation chamber: (a) Top portion (b) Bottom portion (c) Input of compressed dry air and ultrasonic nozzle	54
Figure 20: Sample of optical microscope image used for sizing length of individual HARPs	59
Figure 21: Sample of scanning electron microscope (SEM) image of HARPs for measurement of diameters at 10000x magnification	60
Figure 22: Peclet numbers for relative humidities ranging from 0% to 100%.....	64
Figure 23: Schematic of a quarter circle slice from a droplet with a uniform distribution of particles	66
Figure 24: Concentration distribution for a collapsed spherical droplet with a uniform distribution of particles.....	67
Figure 25: Schematic of a quarter circle slice of a shell-like concentration distribution..	68
Figure 26: Concentration distribution for a collapsed spherical droplet with a shell-like structure.....	69
Figure 27: 3D Visualization of concentration distribution of a 2D circle resulting from a crushed spherical shell.....	69
Figure 28: Concentration distribution for a collapsed spherical droplet with a shell-like structure of varying thicknesses	70
Figure 29: Optical microscope images for determining the CML: (a) before measurement (b) after measurement and mark up	71
Figure 30: SEM image of particles generated with 0.5 mg/ml of CA and ambient air at 18.1 l/min at 200x magnification	74
Figure 31: SEM image of particles generated with 0.5 mg/ml of CA and ambient air at 18.1 l/min at 1000x magnification	75
Figure 32: SEM image of particles generated with ambient air at 10.9 l/min at 60x magnification	76
Figure 33: SEM image of particles generated with dry air at 14.7 l/min at 1500x magnification	78
Figure 34: SEM image of particles generated with dry air at 7.4 l/min at (a) 120x magnification and (b) 1200x magnification	79
Figure 35: SEM image of particles generated with dry air at 1.0 l/min at 300x magnification	80
Figure 36: SEM image of CA particles of 2.0 mg/ml generated with dry air at 15.0 l/min at (a) 300x magnification and (b) 3000x magnification	81
Figure 37: SEM image of CA particles of 2.0 mg/ml generated with dry air at 15.0 l/min 1000x magnification.....	82
Figure 38: Division of inner and outer areas of Figure 37	83

Figure 39: SEM image of CA particles of 0.5 mg/ml generated with dry air passed through an orifice at 16.0 l/min at 1000x magnification 85

Figure 40: SEM images of CA particles of 0.5 mg/ml generated with dry air passed through an orifice at 16.0 l/min at 2000x magnification 86

Figure 41: SEM image of CA particles of 0.5 mg/ml generated with dry air passed through an orifice at 16.0 l/min at 6000x magnification 87

Figure 42: SEM image of two CA particles of 0.5 mg/ml generated with dry air passed through an orifice at 16.0 l/min at 3000x magnification 88

Figure 43: SEM image of CA particles of 0.5 mg/ml generated with dry air passed through an orifice at 16.0 l/min at 3000x magnification 89

1 Introduction

1.1 Inhaled Pharmaceutical Aerosols

Pharmaceutical aerosols remain a growing field of interest in developing new methods of delivering therapeutic agents to the body. The large surface area of the lung offers excellent possibilities as a portal for fast and efficient drug delivery. Currently, local drug delivery to the lung is common for the treatment of diseases such as asthma and chronic pulmonary infections. As opposed to oral or intravenous delivery, the use of inhaled pharmaceutical aerosols allows drug concentrations at the site of interest to be more easily achieved, while systemic drug concentrations can be reduced [1]. For small molecules, this is the second fastest method of drug delivery, making respiratory drug delivery a favourable choice for systemic drug delivery as well [2].

1.2 Lung Cancer and Inhaled Chemotherapy

More recently, inhaled pharmaceuticals have become of interest for the treatment of lung cancer [3-5]. Not only is this disease prevalent, but has one of the lowest survival rates among major cancers [6]. One of the major obstacles in the treatment of lung cancer is the inability to deliver adequate therapeutic drug concentrations to the site of the tumor [5]. The use of inhaled chemotherapy in the treatment of lung cancer attempts to overcome this problem. Drug concentrations in the lung can be greatly increased without causing systemic toxicity as the drug would be delivered directly to the lung as opposed to being delivered intravenously through the circulatory system. This results in greater drug concentrations in the lung and a decrease in the systemic side effects experienced by the patient [4]. These benefits could be even further

extended if the drug could be targeted to increase concentrations locally within the lung at the site of the cancer. Through the use of non-invasive magnetic targeting this has been shown possible in mice [7]. However, the ability to scale up the magnetic field for use in humans is limited [8]. Martin and Finlay have explored an alternative non-invasive magnetic targeting approach whereby the orientation of high aspect ratio particles (HARPs) loaded with iron oxide nanoparticles are controlled to locally increase deposition within the lung [9-11]. This method eliminates the issue of scaling up the magnetic field but still presents the same advantages of targeted drug delivery.

1.3 Summary of Thesis

Targeting via magnetic alignment of HARPs loaded with iron oxide nanoparticles has shown great promise in an *in vitro* study previously done by Martin and Finlay [10]. Through alignment of these HARPs in an array of airway bifurcations, deposition was increased by 1.7 times [10]. To further develop this method of targeted drug delivery both an *in vivo* study and a feasibility analysis into the optimization of the shape of these HARPs were completed.

For the *in vivo* study, New Zealand white rabbits were selected to determine the increase in aerosol deposition in a lung targeted with the application of a magnetic field. The iron oxide nanoparticles also functioned as a magnetic resonance imaging (MRI) contrast agent, allowing the signal intensity of MRI images taken to be related to the concentration of iron [12]. This data was then used to calculate iron concentrations in the lungs of targeted and non-targeted rabbits, which were compared to show regional differences in deposition [13].

Further investigation into the feasibility of creating longer HARPs for improving this method of targeted drug delivery was also completed. For this study the focus was on creating larger water droplets, which were thought to have previously limited the length of the HARPs created. To create these larger droplets, an ultrasonic nozzle was selected. The droplets were then dried in a large evaporation chamber. The aerosol was then collected for both optical microscope and scanning electron microscope (SEM) imaging. The influence of several variables on the drying efficiency and final particle morphology were investigated.

2 Background

2.1 Characteristics of the Respiratory Tract

The adult human lung delivers oxygen to all the cells of the human body with its large surface area of approximately 130m^2 for gas exchange, which is nearly the size of a tennis court [14]. The respiratory tract can be imagined to be similar to a tree, with a trunk splitting into smaller branches, which continue to split into smaller and smaller branches until finally reaching the leaves of the tree. The conducting airways of the respiratory system can be thought of much like these branches, with the leaves representing the alveoli, the primary location of gas exchange.

Three main sections comprise the respiratory tract: The extra-thoracic region, the tracheo-bronchial region, and the alveolar region. When referring to areas of the respiratory tract, the term distal indicates regions that are deeper in the lung, such as the alveolar region and the term proximal indicates areas that are closest to the mouth and throat. The extra-thoracic region is the most proximal component of the respiratory system and includes: the oral cavity, the nasal cavity, the pharynx and the larynx. The tracheo-bronchial section represents the bifurcating airways which conduct air from the extra-thoracic region down into the alveolar region where gas exchange occurs.

Upon beginning inspiration, the air enters through the extra-thoracic region and moves into the tracheo-bronchial region. Once passing through the trachea, the airway splits into the two main bronchi which separate the air into the left and right lungs. From here the airway splits into the lobar bronchi, which divides the airflow again for delivery to the 5 lobes of the lung (3 in the right lung, 2 in the left lung). At this point, the

airways continue to split dichotomously, with each parent airway forming two smaller daughter airways. The tracheo-bronchial region shifts into the alveolar region after passing through the terminal bronchioles. After this point, the airway passages begin to have alveoli on their walls for gas exchange. These respiratory bronchioles continue to branch, with more alveoli on each subsequent respiratory bronchiole until they become alveolar ducts, where the walls are completely covered in alveoli [15]. This long series of branching channels end in the 300 million alveolar sacs, where the majority of gas exchange takes place [14]. Each time the airway branches, this new level is referred to as a generation. The trachea is generation zero, the main bronchi are generation one, the lobar bronchi are generation three, and so forth until finally reaching the final generation in the alveolar sacs.

The airways of the respiratory system are lined with epithelial cells, which act as a barrier between the air and the blood stream, much as skin acts as a barrier for the exterior of the body. In the conducting airways this epithelium is covered in a layer of mucous which collects the particles which enter the respiratory system, acting as a filter. This mucous layer is constantly being moved upwards by fine hairs on the epithelium called cilia, towards the extra-thoracic region where the mucous is either coughed up or swallowed [15]. Once a particle reaches the alveolar sac, a different method of removing particles is used. Particles that reach this depth are instead consumed by phagocytes which reside in the alveolar sacs of the lung [16].

In order to perform computational analysis, or in vitro testing, an idealized model of the lung is desirable. In reality, not all branching is dichotomous, and the lengths and diameters of each generation of the airway are not identical [17]. However, with the

large number of airways present in the lung, an idealized, symmetrical branching model can be used to approximate the geometry of the lung. The Weibel A is one of the original airway models giving diameters and lengths for 23 generations of the lung [18]. Finlay et al have altered this model by adjusting the geometries of the airways slightly to account for a more realistic lung volume of 3l instead of the 4.8l which is used in the original Weibel A model [19]. The geometries of the Finlay et al model can be seen below in Table 1.

Table 1: Airway diameters and lengths for each generation from Finlay et al [19]

	Generation	Airway Diameter (cm)	Airway Length (cm)
Tracheo-Bronchial Region	0	1.81	12.456
	1	1.414	3.614
	2	1.115	2.862
	3	0.885	2.281
	4	0.706	1.78
	5	0.565	1.126
	6	0.454	0.897
	7	0.364	0.828
	8	0.286	0.745
	9	0.218	0.653
	10	0.162	0.555
	11	0.121	0.454
	12	0.092	0.357
	13	0.073	0.277
14	0.061	0.219	
Alveolar Region	15	0.049	0.134
	16	0.048	0.109
	17	0.039	0.091
	18	0.037	0.081
	19	0.035	0.068
	20	0.033	0.068
	21	0.03	0.068
	22	0.028	0.065
	23	0.024	0.073

2.2 Aerosol Deposition in the Lung

2.2.1 Aerosol Particle Motion

The motion of an aerosol particle in a fluid flow is dependent on multiple forces exerted on the particle simultaneously. This can result in complications in attempting to determine the trajectory of a single particle [1]. However in the case of pharmaceutical aerosols, where often the particles are very small and density of the particle (ρ_p) is much greater than the density of the fluid (ρ_f), the force of drag on the particle is much larger than the other fluid forces present [20].

The force of drag can be simplified down to Stokes law [21]:

$$F_{\text{drag}} = -3\pi d\mu(v - v_{\text{fluid}}) \quad (1)$$

where d is the particle diameter, μ is the dynamic viscosity of the fluid, v is the velocity of the particle, and v_{fluid} is the velocity of the fluid. If the diameter of the particles is very small, the Cunningham slip correction factor (C_c) must be applied [22]. When particles are in the same size range as the mean free path of the fluid, the continuum assumption of the fluid no longer applies. The mean free path of the fluid represents the average distance travelled by a fluid molecule prior to colliding with another molecule.

Another parameter of interest for pharmaceutical aerosols is the particle settling velocity. In still air particles will settle under the force of gravity. These particles will quickly reach their terminal velocity, where the force of drag exerted on the particle is equal to the force of gravity. Assuming these are the only two forces exerted on the particle, the settling velocity can be determined from the simple force balance:

$$mg = F_{\text{drag}} \quad (2)$$

Where the mass of the particle is $m = \rho_p V$ and V is the volume of the particle. For a spherical particle and using Stokes law, the terminal settling velocity (v_{settling}) can be defined as:

$$v_{\text{settling}} = \frac{\rho_p g d^2}{18\mu} \quad (3)$$

The settling velocity is of special interest in pharmaceutical aerosols to help predict where and how particles will deposit within the respiratory tract [1].

2.2.2 Mechanisms of Deposition

To predict where and how aerosols are deposited in the lung is important in determining necessary doses and optimizing drug delivery systems when developing methods of drug delivery [1]. Deposition within the respiratory system is dominated by three main mechanisms: inertial impaction, sedimentation, and diffusion. Impaction occurs when the particle possesses too much inertia and cannot follow the streamlines of the flow around a turn within the airways (such as a bifurcation), and instead impacts the wall of the airway. This mechanism is dominant for deposition in the extra-thoracic region and the more proximal generations of the tracheo-bronchial region where there are higher air flow velocities. Sedimentation occurs when the force of gravity on the particles causes them to settle and deposit on the airway wall. This mechanism becomes important deeper in the lung in the alveolar region. Diffusion causes deposition when small particles are being considered, as the force of the air molecules hitting the particle can cause it to move due to Brownian motion and deposit onto the airway wall [1].

These mechanisms do not work independently but combine to create a pattern of deposition in the various generations of the lung for given droplet sizes. Stahlhofen et al showed this experimentally by comparing fast and slow-cleared thoracic deposition of radioactive labeled particles with aerodynamic diameters above 0.1 μm [23]. The aerodynamic diameter is the diameter of a spherical particle of unit specific gravity which would exhibit the same aerodynamic properties as the particle of interest. The fast-cleared deposition approximates deposition in the tracheo-bronchial region, as these particles would be cleared within a day or so from the respiratory system and the slow-cleared deposition is representative of deposition in the alveolar region, taking much longer to exit the respiratory system. Particles with a diameter of approximately 10 μm are most likely to deposit in the trachea-bronchial region due to inertial impaction. Particles larger than this are mostly filtered out in the extra-thoracic region. For slow-cleared deposition, representative of the alveolar region, there is a significant increase in the deposition of particles with diameters up to 5 μm , due to gravitational settling [23]. However, it is important to note that some of the deposition in the tracheo-bronchial region will be part of this slow-cleared deposition.

2.2.3 Deposition of HARPs

The deposition of high aspect ratio particles (HARPs) is governed by a different mechanism of deposition: interception. Interception occurs when a part of the particle collides with the wall while the center of mass of the particle remains in the streamline [24]. The importance of interception in the deposition of HARPs is due to a number of factors. Asbestos fibers of lengths up to 200 μm can be found in the alveolar region of the lung, whereas spherical particles greater than 10 μm in diameter rarely penetrate this deep into the lung [25]. Jeffrey has shown that as HARPs flow through a fluid they

tumble with a trajectory now called Jeffrey's motion where the angular velocity while parallel to the streamlines is much slower than when the particle is perpendicular [26]. This phenomenon was seen by Myojo, who observed the deposition of glass fibers deposited in an airway bifurcation and found the deposited fibers tended to align parallel to the flow [27]. This behavior would explain the ability of these HARPs to get much deeper into the lung than spherical particles. As the HARPs travel through the lung, their orientation tends to be parallel to the airway walls, decreasing deposition by interception. Additionally, deposition of HARPs by interception depends primarily on the particle diameter, where the diameters are on the order of 1 μm , and not on the length [28]. In the context of pharmaceutical aerosols, the mass of drug delivered is of primary interest. By increasing the lengths of HARPs while maintaining a small diameter, higher masses of drug can be delivered deeper into the lung.

2.3 Applications of pharmaceutical aerosols

Drugs can be delivered to the body through a variety of methods such as: orally, intravenously, or through the respiratory system. The large surface area of the lung offers great possibilities for fast and efficient drug delivery both systemically and locally.

Local drug delivery is in common use for treatment of diseases occurring within the lung itself such as asthma and chronic pulmonary infections, commonly found in patients with cystic fibrosis. Because the drug is being delivered directly to the site of disease or infection, there are higher drug concentrations at the site of interest, and systemic side effects can be reduced [4]. This direct delivery wastes less drug, resulting in a more cost-effective solution. However, the development of an effective drug delivery system incurs an added cost to drug development [1]. Also, breathing patterns and inhalation

rate can dramatically affect how and where the drug deposits in the lung [1,29]. By taking a very fast rapid breath with inhalation, the inertial impaction of the particles will increase, leading to most of the particles being deposited in the mouth and throat, whereas a slow breath would lead to more particles reaching the deeper parts of the lung. Because of this, inter-subject variability of dosing is difficult to control, and technique of inhalation is important.

Using the lung for systemic delivery of drugs is not a commonly used practice. However, this method can offer effective and rapid drug delivery [30]. Drugs delivered through the lung are less likely to be degraded than if delivered orally, due to the lower concentrations of drug-metabolizing enzymes present in the lung [31]. For small molecules, this is the second fastest method of drug delivery, partly because of the decreasing mucous thickness found deeper in the lung [2]. However, this rapid effect is not always desirable when slow absorption for a prolonged systemic effect is needed. It is also important to ensure the drugs are deposited in the optimal location in the lung for absorption. Curry *et al* showed that smaller particles (aerodynamic diameter of 2 μm) absorb more readily into the blood stream than larger particles (aerodynamic diameter of 11.7 μm) because of the penetration of the smaller particles deeper into the lung [32]. Another factor to consider is patient compliance and satisfaction. In the case of diabetes where insulin is delivered subcutaneously with a needle, the convenience of an inhaled insulin led to 85% of patients choosing it over the traditional means of delivery [33].

More recently, inhaled pharmaceuticals have become of interest for the treatment of lung cancer [3-5]. In Canada it is estimated that in 2010 24,200 patients will be

diagnosed with lung cancer, and 20,600 will die from it [6]. Not only is this disease prevalent, but has one of the lowest survival rates among major cancers [6]. In the treatment of lung cancer, one of the major obstacles is the inability to deliver adequate therapeutic drug concentrations to the site of the tumor [5]. The use of inhaled chemotherapy in the treatment of lung cancer attempts to overcome this problem. Drug concentrations in the lung can be greatly increased without causing systemic toxicity, which results in greater drug concentrations at the site of interest and a decrease in the systemic side effects experienced by the patient [4]. The cytotoxic effect of the drug may result from direct topical application to the tumour, as well as absorption of the drug into the bronchial circulation which supplies blood to the tumour. In addition, tumours will often locally destroy the bronchial cilia, which in the case of aerosol delivery aids in retaining the drug at the desired site over a longer period of time [3]. In addition to the benefits of inhaled chemotherapy, Geng *et al* found that HARPs offer an additional boost to the effectiveness of the anticancer drug paclitaxel when delivered intravenously [34]. The effectiveness of the drug was further increased as the length of the particles increased. It is possible that by having the drug absorbed into the bronchial circulation, this effect could also be seen through the use of inhaled chemotherapy. By implementing inhaled chemotherapy with the advantages of HARPs, the effectiveness of anti-cancer medication for lung cancer could be further improved.

2.4 Targeted aerosol drug delivery

2.4.1 Previous work

The ability to control where drugs are deposited within the lung is a growing field of interest. This includes not only controlling how deep the drugs penetrate into the lung,

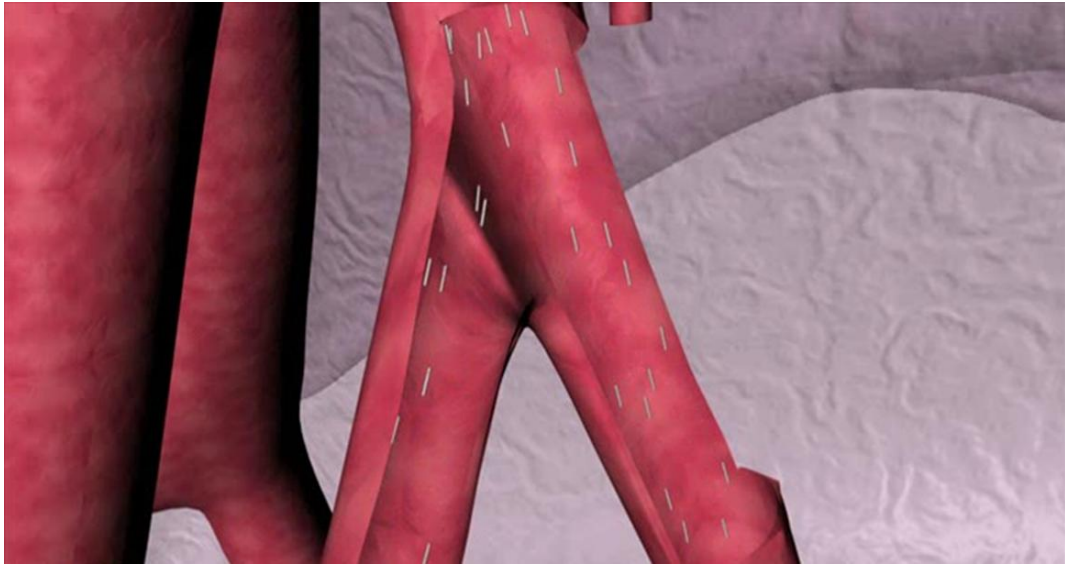
but also being able to target certain sites locally within the lung. Utilizing this technique would allow for less of the drug to be delivered where not necessary, decreasing side effects and also cost of treatment. There are a variety of methods to target a selected range of generations within the lung, including optimizing the particle density or size, or varying the inhalation flow rate [1,16,35]. By creating particles with diameters of 1-3 μm , the alveolar region can be targeted allowing for better uptake of drug for systemic delivery [1]. Alternatively, Edwards *et al* were able to decrease particle density by creating larger porous particles, which were able to be delivered deeper in the lung for effective drug delivery [16]. By decreasing the inhaled flow rate, Camner *et al* were able to deliver particles deeper into the lung than at normal inhalation flow rates [35]. Although these methods are somewhat effective at targeting regions of the lung, they are not able to locally target specific sites within the lung, which would be of interest for a disease such as lung cancer where often only one lobe of the lung is affected.

There have been several different approaches aimed at tackling the problem of site specific targeted drug delivery. One of these methods utilized an intratracheal nebulizing catheter to aerosolize the drug inside the lobe or lung to be targeted. Although this method has been shown to be effective in dogs [36], it's an invasive procedure with additional health risks. In contrast, Dames *et al* [7] have investigated a non-invasive method of magnetically targeted drug delivery in mice through the use of nebulized droplets containing superparamagnetic iron oxide nanoparticles. They found an increase in deposition of 7.9 times with the tip of an electromagnet centered 1mm above the surgically exposed right lobe of the lung. Although this is a promising result, several complications could arise in attempting to apply this procedure for humans. Importantly, when moving the magnet tip to 5mm away from the target site, the

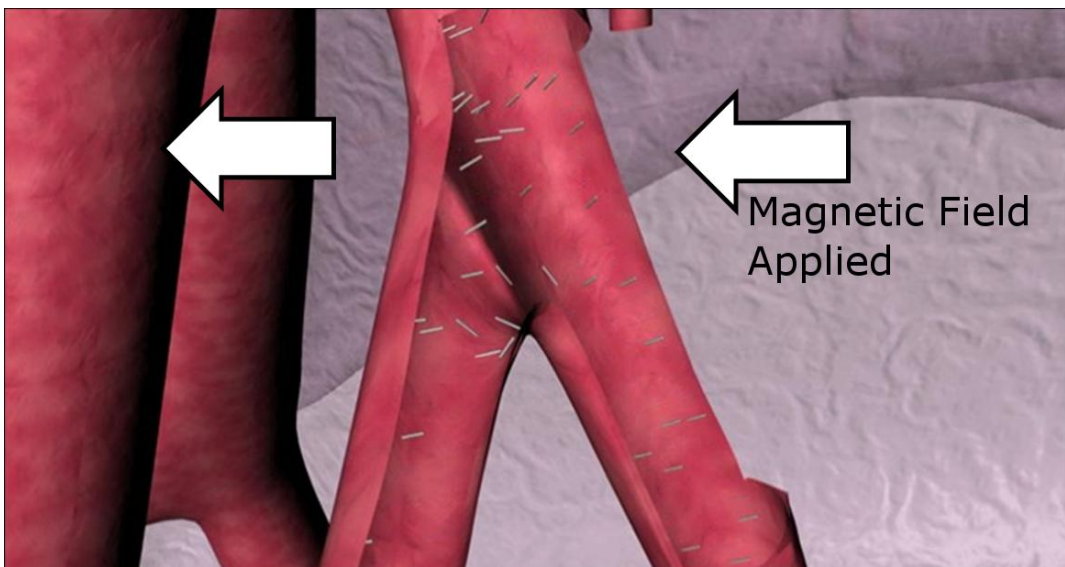
magnetic flux decreased by approximately 90% [7]. Study into the design of magnetic fields for the purpose of magnetic drug targeting have shown that it remains feasible for superficial sites, but the rapid reduction in magnetic flux with distance from the source makes it a difficult method for targeting tissues deeper in the body without the use of surgically implanted ferromagnetic stents [8]. An alternative noninvasive approach to magnetic targeting in the lung is to utilize high aspect ratio particles (HARPs) in conjunction with superparamagnetic nanoparticles to target specific areas within the lung by controlling particle orientation with the use of a magnetic field [9-11].

2.4.2 Magnetic Targeting with HARPs

The probability of deposition of HARPs is highly dependent on their orientation as they travel through the airways. HARPs will tend to align with their long axis parallel to the direction of flow, as seen in Figure 1(a), for which the probability of deposition is at its lowest [27]. As the tracheobronchial region transitions into the alveolar region, the dominant mechanism of deposition becomes interception. Airways are oriented in a random fashion within the lung. By aligning the HARPs in one direction, the particles would become randomly oriented with respect to the direction of flow in the airways, leading to a higher probability of deposition [37]. By loading HARPs with superparamagnetic nanoparticles a preferred axis of magnetization is created along the length of the particle [11]. By placing a select region of the lung in a magnetic field, the orientation of the particles can be controlled by using the magnetic torque to align the long axis of the particles in the direction of the field, as seen in Figure 1(b). Martin and Finlay investigated the feasibility of this technique and found the magnetic torque exerted on the particle was enough to overcome the shear forces of fluid flow in the lung for the range of particle aspect ratios of interest [11].



(a)



(b)

Figure 1: Alignment of HARPs in the lung (a) naturally (b) in the presence of a magnetic field

This was demonstrated in vitro by Martin and Finlay with a decrease in the penetration efficiency through a 5 μm polycarbonate membrane filter (Isopore TMTP; Millipore, Billerica, MA) [9]. It was found that by creating a magnetic field perpendicular to the airflow at the filter, approximately 4 times more particles deposited on the filter. This was further confirmed using an airway model representative of the terminal bronchioles

of the lung [10]. Martin and Finlay showed an increase in deposition of cromoglycic acid (CA) HARPs of approximately 1.7 times with the application of a magnetic field compared to without [10]. The HARPs with and without magnetite had volume median diameters (VMDs) of 0.47 and 0.32 μm respectively and volume median lengths (VMLs) of 3.0 and 2.0 μm respectively [10]. Although (CA) is not intended for cancer therapy, it was chosen as a model drug, as it forms acicular crystals. The anticancer drug paclitaxel has been loaded onto HARPs and shown to be more effective at shrinking tumours in this shape [34].

3 Pilot study of inhaled aerosols targeted via magnetic alignment of HARPs in rabbits

3.1 Introduction

Targeting via magnetic alignment of HARPs has shown promise in an *in vitro* study previously done by Martin and Finlay [10]. Through alignment of these HARPs in an array of airway bifurcations, deposition was increased by 1.7 times [10]. To follow up on this promising result an *in vivo* study was completed to further develop this method of targeted drug delivery in the lung.

New Zealand white rabbits were selected to determine the increase in aerosol deposition in a lung targeted with the application of a magnetic field. The use of laboratory animals for the study of inhaled particle deposition is common, as the total and regional particle deposition is qualitatively similar to humans [38]. The signal intensity of the images could be related to the concentration of iron since the iron oxide nanoparticles also functioned as a magnetic resonance imaging (MRI) contrast agent [12]. This data was then used to calculate iron concentrations in the lungs of targeted and non-targeted rabbits, which were compared to show regional differences in deposition [13].

3.2 Methods

3.2.1 Aerosol Production

HARPs of cromoglycic acid (CA) were prepared following the crystallization method of Chan and Gonda [39] using cromolyn sodium salt purchased from Sigma-Aldrich Canada (Oakville, ON). To create one dose of suspension for nebulization, 10 mg of CA was combined with 150 μ l of colloidal super paramagnetic iron oxide, FeREX (BioPAL,

Worcester, MA), and 5 ml of deionized water. The FeREX had a concentration of 10 mg Fe/ml. Dried CA particles and FeREX were dispersed by pipette to form an aqueous suspension prior to nebulization. These suspensions were nebulized using a clinically marketed vibrating mesh nebulizer (Aeroneb Pro; Aerogen, Galway, Ireland) and subsequently dried using a diffusion dryer containing silica gel (Component of Model 3475 Monodisperse Aerosol Generator; TSI, Shoreview, MN). This resulted in HARPs, similar to those previously created for an in vitro study, with diameters on the order of 500 nanometers and lengths varying from 1 to 10 micrometers [10]. The FeREX particles were specified to be in the range of 50 – 150 nm by the manufacturer. An SEM image taken of the HARPs generated can be seen in Figure 2. These HARPs were collected on a 0.2 μm polycarbonate membrane (Isopore GTTP04700; Millipore, Billerica, MA) with a magnetic field produced with permanent magnets across the face of the membrane to demonstrate alignment.

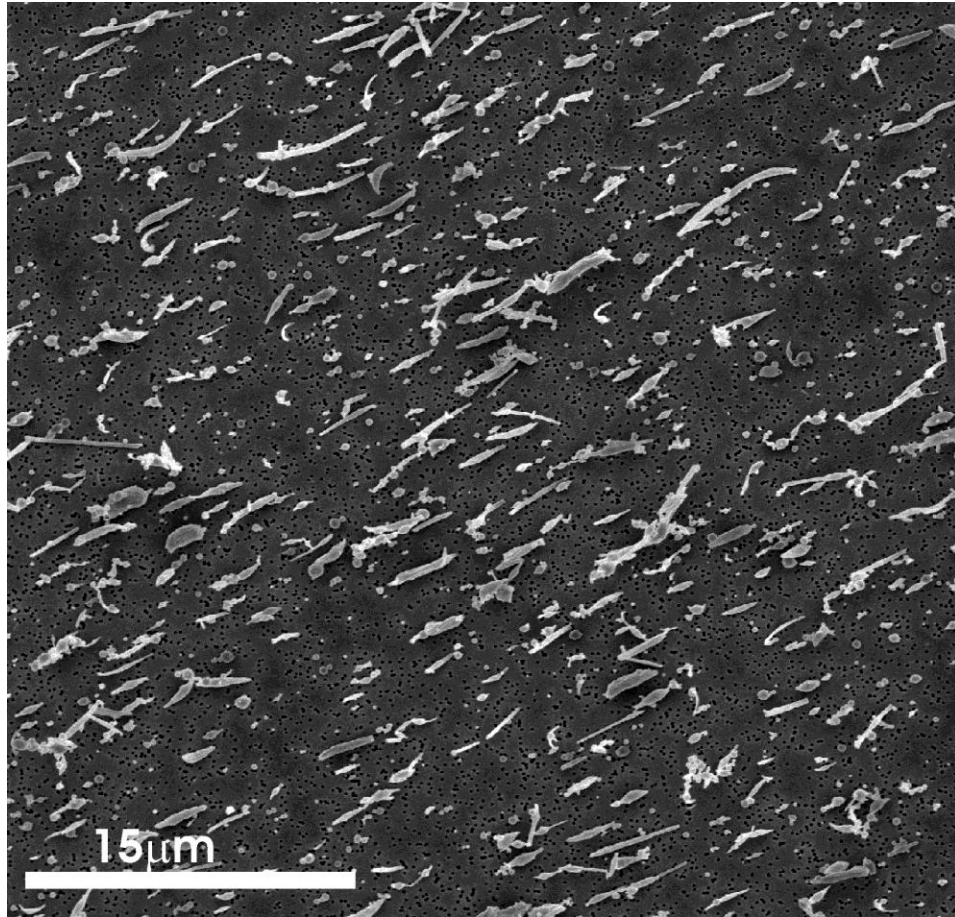


Figure 2: SEM image of high aspect ratio particles (HARPs) of CA and FeREX. The light coloured aligned particles are the HARPs and the small black dots are the pores of the membrane.

In order to ensure that regional lung distributions of iron are representative of regional distributions of CA throughout the lung, the distribution of iron across the range of HARP sizes was examined. This was done by drawing aerosol from the nebulizer and diffusion dryer through a cascade impactor (Mark II Andersen Impactor; Thermo Andersen, Smyrna, GA) at 28.3 l/min. UV spectrophotometry was used to determine the masses of CA and iron deposited on each stage of the impactor. The mass of CA was found by washing with 0.01 N sodium hydroxide and assaying by UV spectrophotometry at a wavelength of 326 nm. The mass of the iron was determined by methods similar to those described previously by Suwa *et al* [40]. Prior to spectrophotometry at 468 nm,

the water insoluble FeREX was transformed to soluble Fe^{3+} using concentrated hydrochloric acid and the CA was removed from suspension with the use of a 0.8 μm filter.

3.2.2 Animals

This study involved 19 male New Zealand White Rabbits with weights ranging from 3.4 to 4.5 kg. The animals were housed under conventional conditions under the guidelines of the Canadian Council on Animal Care for one week prior to the study. All animal procedures were approved by the University of Alberta Health Sciences Animal Policy and Welfare Committee.

3.2.3 Exposure

The nebulizer and diffusion dryer were added to the inspiratory line of a mechanical ventilation circuit (InfantStar; Infrasonics Inc., San Diego, CA) to deliver the aerosol to the lungs of ventilated rabbits. This circuit is outlined below in Figure 3 where the rabbit lung is ventilated via a 3.5 mm endotracheal tube. All excess aerosol (not deposited in the respiratory system of the rabbit) was collected on a filter (Respirgard; Vital Signs, Totowa, NJ) in the expiratory line. After the animals were anesthetized using intravenous ketamine and xylazine infusions, a tracheostomy was performed and a 3.5 mm endotracheal tube was inserted, connecting the rabbit to the mechanical ventilation circuit. The animals were then paralyzed using a pancuronium (0.2 mg/kg) intravenous infusion. All drug infusions were repeated as needed. Mechanical ventilation was performed using 100% oxygen with a peak inspiratory pressure of 14 cm H_2O , a positive end-expiratory pressure of 2 cm H_2O , a continuous flow of 6 l/min, and an inspiratory time of 0.5 s. The oxygen was neither warmed nor humidified prior to

inspiration. Blood gases were monitored at interval throughout ventilation by arterial blood sampling and analyzed by ABL500 (Radiometer, Copenhagen, Denmark). To maintain an arterial PCO_2 between 40 ± 5 mm Hg, the breath frequency was adjusted between 20 and 25 breaths/min.

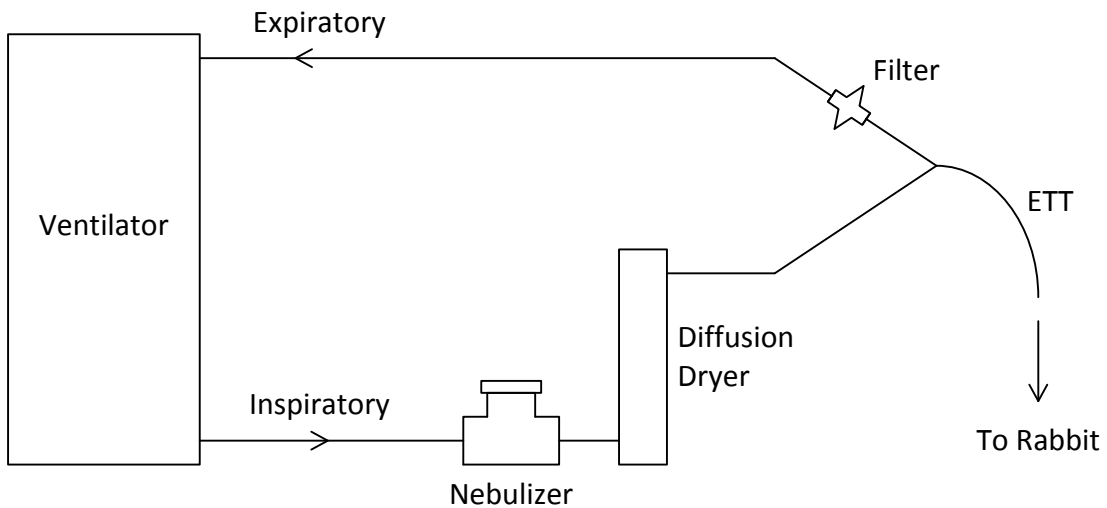


Figure 3: Schematic of mechanical ventilation circuit used to expose rabbits to aerosol. ETT = endotracheal tube.

The animals were separated into three different categories of exposure: 1) no aerosol delivered, 2) aerosol delivered with no magnetic field applied, and 3) aerosol delivered with the application of a magnetic field. Three rabbits were mechanically ventilated for approximately 30 minutes but were not exposed to aerosol. Eight rabbits were exposed to two doses of the aerosol described above. Upon the completion of nebulization of the first dose, the reservoir in the nebulizer was refilled without opening the breathing circuit, and the second dose then ran to completion. The final eight rabbits were exposed to the aerosol but additionally had a magnetic field applied over the right lung.

This was accomplished with the use of neodymium permanent magnets (two stacks of three, 2" x 2" x 0.5" magnets; Indigo Instruments Waterloo, ON). The two stacks of magnets were separated by 20 cm, and positioned above and below the rabbit to create a field strength and gradient which decreased from approximately 35 mT and 1.5 T/m, respectively, at the posterior side of the right lung to 20 mT and 0.1 T/m at the anterior side. In this position, magnetic field lines ran parallel to the direction of gravity, and the field gradient was directed so that small translational magnetic forces acting on particles augmented, rather than subtracted from, the force of gravity. The location of the rabbit relative to the permanent magnets used to generate the magnetic field can be seen below in Figure 4.

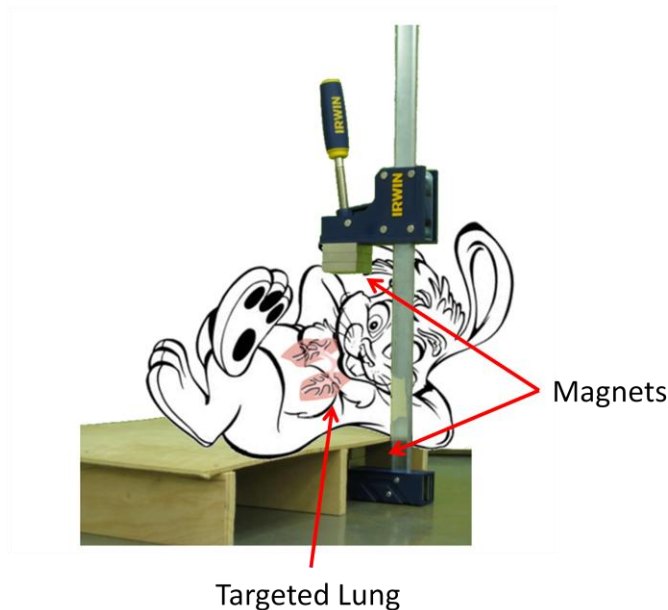


Figure 4: Location of rabbit relative to permanent magnets used to generate magnetic field

For all exposed rabbits ventilation lasted on average for approximately 45 minutes, with aerosol produced on average for approximately 23 minutes. All rabbits were euthanized

with a pentobarbital intravenous infusion upon the completion of ventilation. The time between death and MRI scan was between 40 and 70 minutes for all rabbits.

3.2.4 Measurement of Deposition

The use of an MRI machine allows for detailed visualization of internal structures of the body. This is done through manipulation of the magnetic properties of the hydrogen atoms found within the body. Upon entering the MRI machine, a powerful magnetic field aligns the magnetization of these hydrogen atoms. Then a radio frequency transmitter is briefly turned on, causing some of the aligned protons of the hydrogen atoms to flip their spin. This is done through carefully selecting the frequency of the transmitter to create an electromagnetic field with protons at a specific resonance frequency able to complete this task. Then as these protons decay to their original spin state the magnetization of the tissue precesses which generates a signal as an alternating current in induction coils surrounding the tissue. This signal is detected by the MRI machine which creates an image. Because the protons in different tissues return to their equilibrium states at different rates an image which allows different types of tissues to be distinguished is created.

For this study, MRI measurements were performed using a Siemens Sonata 1.5 T, 60 cm bore system (Siemens Medical Systems, Erlangen, Germany). Each rabbit was oriented in the prone position, in a 16 cm diameter volume birdcage coil, with the lungs placed at the centre of the coil to maximize reception sensitivity and uniformity. Iron oxide functions as an MRI contrast agent [12] which allows the signal intensity of the images to be related to the iron concentration. Specifically, the T_1 relaxation time, which describes the rate of recovery of the magnetization to thermal equilibrium, is directly related to the iron concentration according to the following relationship [40,41]

$$\frac{1}{T_1} = \frac{1}{T_{1,0}} + \alpha \cdot c \quad (4)$$

where $T_{1,0}$ is the baseline relaxation time (determined from the 3 baseline rabbits), c is the tissue concentration of iron, and α is a constant specific to the contrast agent as determined from previous work [13]. The average signal intensity (SI) within each region of interest was corrected for noise using the relationship

$$SI = \sqrt{SI_0^2 - n^2} \quad (5)$$

where SI_0 is the average signal intensity prior to subtraction of the noise, n , measured as the average signal intensity in a region of interest far away from the rabbit. The T_1 and $T_{1,0}$ values were calculated by inverting the MRI signal intensity and then fitting the magnitude of the recovered MRI signal intensity measured at increasing delays following the inversion preparation, as shown below

$$SI = \text{abs} \left[SI_\infty \left(1 - k \cdot e^{-T_i/T_1} \right) \right] \quad (6)$$

where SI is the signal intensity at inversion time T_i , and the constants SI_∞ , k , and T_1 were determined by nonlinear regression. An example of the fit of the data points found from this nonlinear regression is seen below in Figure 5.

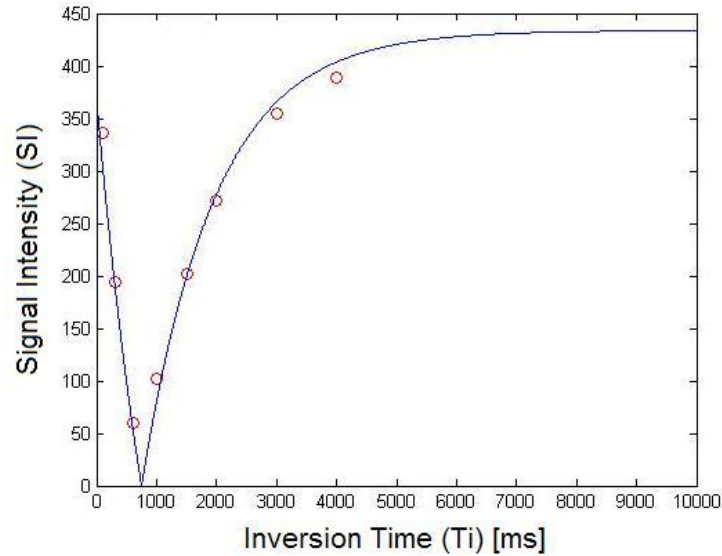


Figure 5: Nonlinear regression fit to SI curve

To acquire the SI values, an inversion-recovery fast spin echo pulse sequence with either 8 or 11 T_i times from 100 to 4000 ms, in addition to the case of no inversion, was used to map the longitudinal relaxation time within the lung. An example of one slice at various T_i times can be seen below in Figure 6. The image parameters were as follows: 108 x 25 mm field of view and a 448 x 105 matrix (in-plane spatial resolution interpolated to 250 x 250 μm). There were 24 2.5 mm thick axial slices taken in two serial experiments (to prevent cross-talk between neighboring slices) which spanned the lung from the apex to the diaphragm. An example of 20 of these slices at an inversion time of 4000 ms can be seen below in Figure 7. The pulse sequence had a repetition time, TR, of 5120 ms and an echo time, TE, of 12 ms. The total acquisition time for each rabbit was approximately 30 minutes.

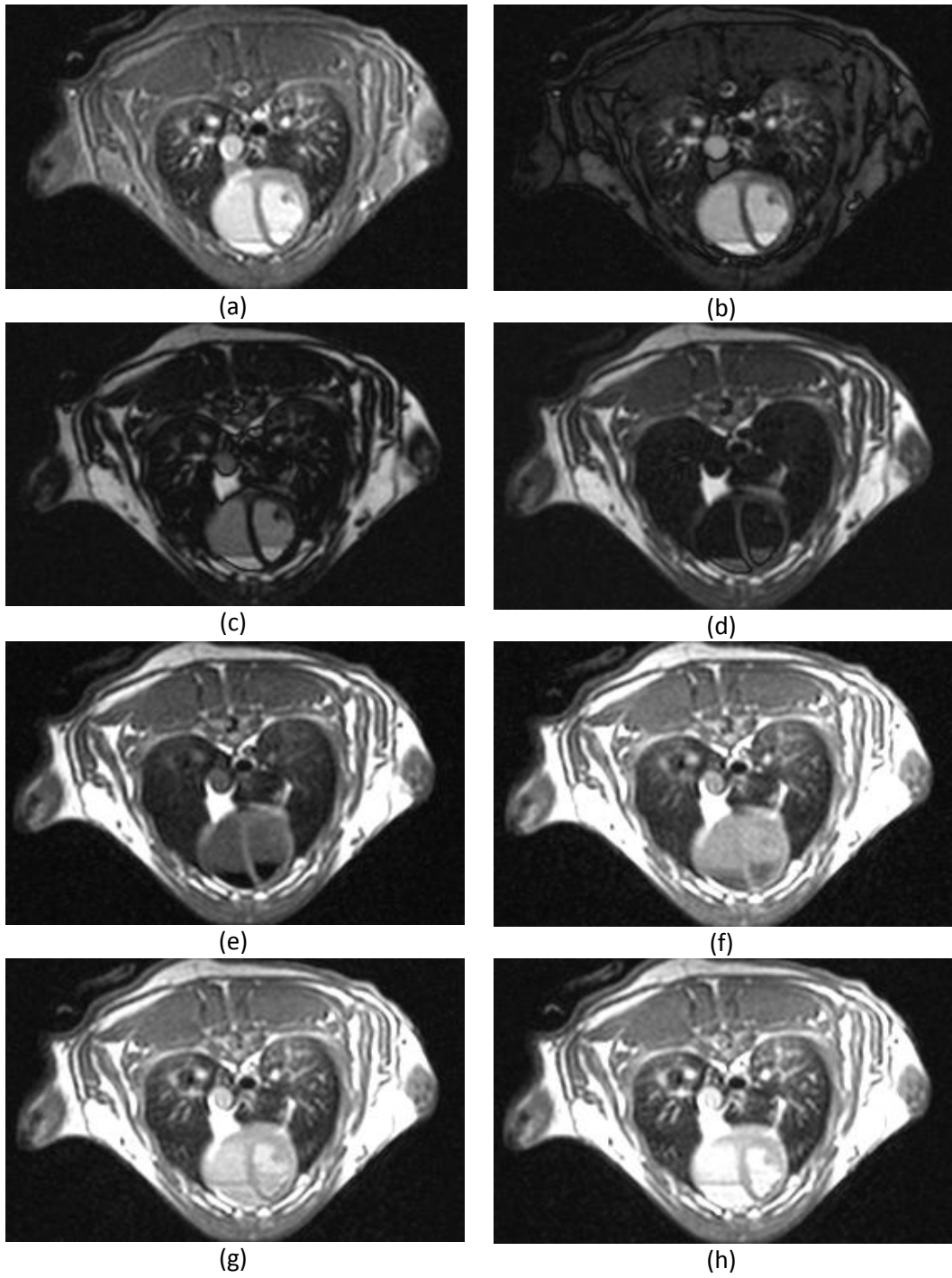


Figure 6: MRI images at various T_1 times: (a) 100 ms (b) 300 ms (c) 600 ms (d) 1000 ms (e) 1500 ms (f) 2000 ms (g) 3000 ms (h) 4000 ms



Figure 7: MRI images at $T_1 = 4000$ ms spanning from the apex to the diaphragm

The images attained from the MRI scans were post-processed to map iron concentrations in the right and left lung for each rabbit. The lungs were manually segmented and regions of high signal strength associated with lung vasculature were removed using a threshold filter as shown in Figure 8. A MATLAB (The Mathworks, Natick, MA) script was written to calculate the average T_1 relaxation times for user-selected regions of interest within the right and left lungs, in apical, medial and basal sub-regions.

Using the regionally calculated T_1 and $T_{1,0}$ values, the iron concentrations were then compared between the right and left lung for each rabbit, globally, and in the , apical, medial, and basal sub-regions. On average 18 of the 24 2.5 mm axial slices spanned the lung from top to bottom, in which case each sub-region was comprised of 6 slices.



(a)



(b)



(c)



(d)

Figure 8: Sample of image processing: (a) original MRI image (b) after selection of region of interest (c) after removal of vasculature (d) iron concentrations in $\mu\text{g}/\text{cm}^3$

3.3 Results

Aerosol drawn through the cascade impactor showed a reasonably even distribution of iron oxide over the size range of CA particles created, ensuring that regional lung distributions of iron were representative of regional distributions of CA. This can be seen below in Figure 9 where statistically significant differences in the iron and CA-weighted size distributions were only seen for the plates 1, 2, and 3.

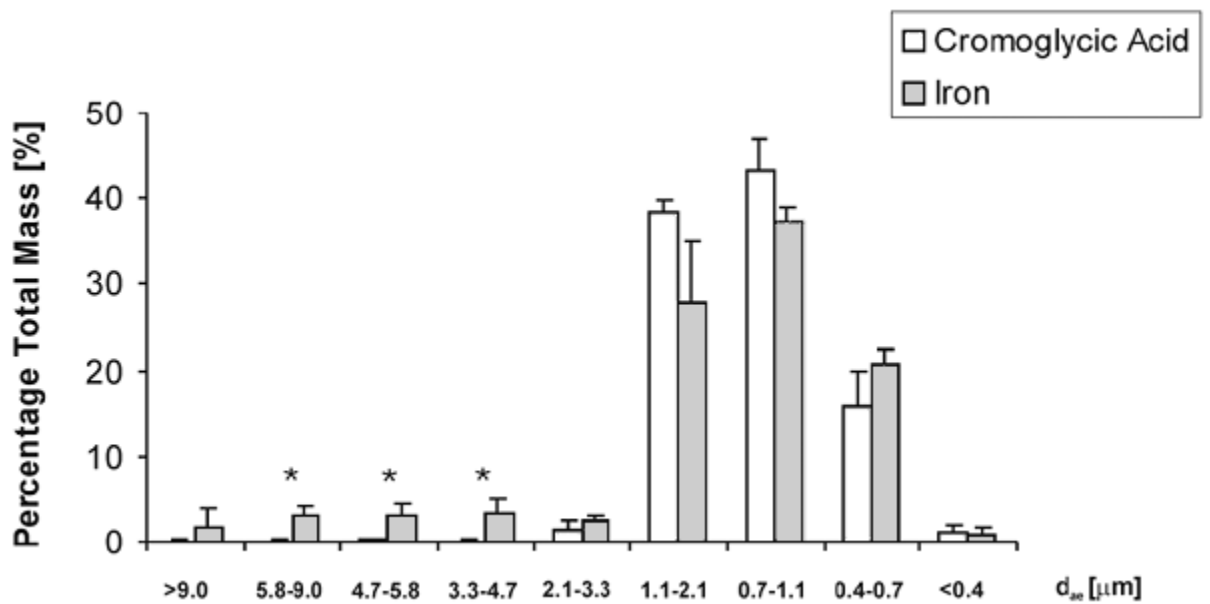


Figure 9: Aerodynamic diameter (d_{ae}) size distributions weighted by mass of iron and mass of cromoglycic acid, as determined by cascade impactation for the iron oxide loaded cromoglycic acid aerosol. Asterisks indicate statistically significant differences between the two distributions ($P < 0.05$; two-tailed student's t-test for independent samples)

For the three baseline rabbits an average $T_{1,0}$ relaxation time of 1531 ± 45 ms was measured. The average whole-lung T_1 relaxation time and iron concentration for the sixteen exposed rabbits were 1211 ms and $1.17 \pm 0.12 \mu\text{g}/\text{cm}^3$ respectively. The T_1 values and iron concentrations for both the left and right lungs of the exposed rabbits are shown in Table 2. The ratio of right to left lung iron concentration was 1.09 ± 0.07

in the non-targeted rabbits and 1.17 ± 0.14 in the targeted rabbits. Non-targeted refers to rabbits exposed without the application of a magnetic field, and targeted refers to those with a magnetic field applied over the right lung.

Table 2: Regional and total area-averaged T_1 relaxation times and iron concentrations for the left and right lung of non-targeted and targeted rabbits

Rabbit	Region	Left Lung		Right Lung		$[Fe]_R/[Fe]_L$
		T_1 [ms]	[Fe] [$\mu\text{g}/\text{cm}^3$]	T_1 [ms]	[Fe] [$\mu\text{g}/\text{cm}^3$]	
<i>Non-Targeted</i>	Total	1206 ± 63	0.61 ± 0.28	1200 ± 60	0.64 ± 0.26	1.09
	Apex	1159 ± 29	0.84 ± 0.15	1140 ± 34	0.95 ± 0.18	1.22
	Middle	1210 ± 28	0.59 ± 0.13	1193 ± 24	0.67 ± 0.11	1.30
	Base	1205 ± 32	0.62 ± 0.14	1225 ± 26	0.52 ± 0.11	0.96
<i>Targeted</i>	Total	1224 ± 44	0.52 ± 0.20	1213 ± 42	0.57 ± 0.18	1.17
	Apex	1178 ± 20	0.73 ± 0.10	1182 ± 28	0.72 ± 0.13	0.94
	Middle	1233 ± 20	0.48 ± 0.09	1205 ± 18	0.60 ± 0.08	1.62
	Base	1216 ± 23	0.56 ± 0.11	1211 ± 19	0.58 ± 0.09	1.18

It can be seen in Figure 10 that with application of the magnetic field, deposition in the targeted lung is decreased in the apical region and increased in the middle and basal regions. When comparing the iron concentration in the middle and base of the lung with the apex of the lung, it can be seen in Figure 11 that in the right lung of the targeted rabbits there is a targeted increase in deposition in the more basal regions.

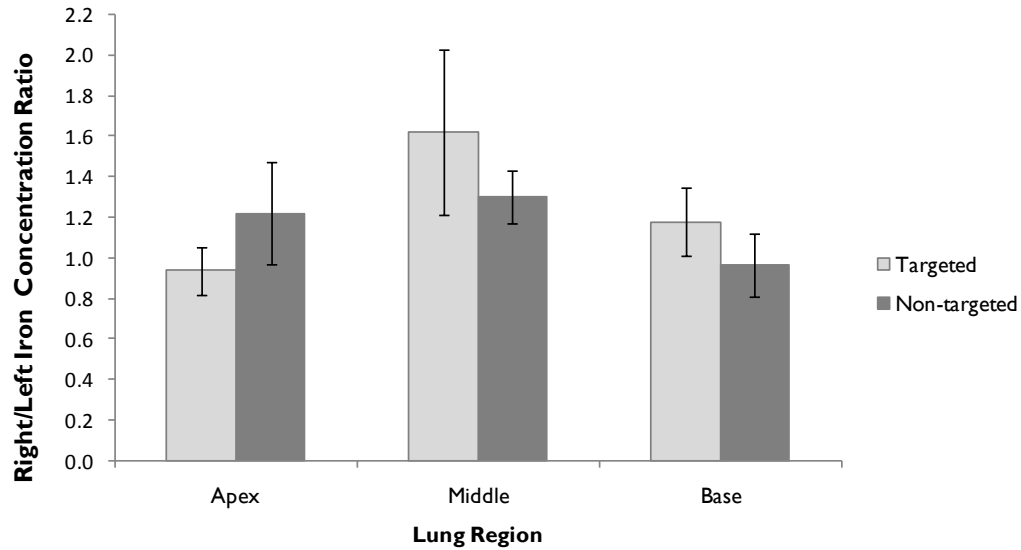


Figure 10: Ratios of regional right to left lung iron concentrations in targeted and non-targeted rabbits. Error bars represent standard errors of the mean

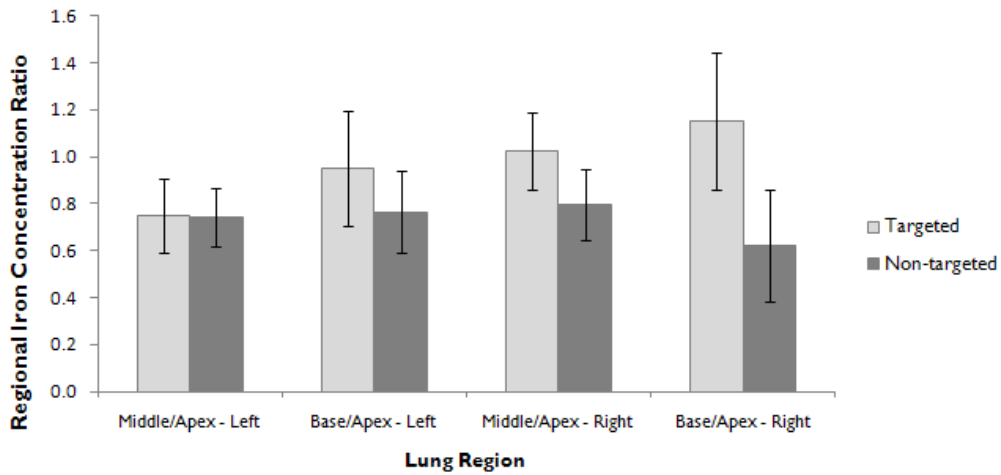


Figure 11: Ratios of iron concentration between middle and apical, and basal and apical regions of the left and right lungs of targeted and non-targeted rabbits. Error bars represent standard errors of the mean

3.4 Discussion

With the right lung being targeted, an increase in the ratio of the right to left lung iron concentrations was expected. After post-processing the images from the 19 rabbits, it was found that the ratio of right/left iron concentration of the untargeted rabbits was

similar to that of the targeted rabbits, which were 1.09 and 1.17 respectively. However, examining the data in more detail, a larger increase in deposition in the middle and basal regions of the lung can be seen. In the middle region of the lung the ratio of right to left lung deposition increased from 1.30 ± 0.13 to 1.62 ± 0.41 and in the basal region deposition increased from 0.96 ± 0.16 to 1.18 ± 0.17 .

CA particles were loaded with iron oxide for the purpose of magnetic alignment, but also acted as an MRI contrast agent. As was seen in there were statistically significant differences in the iron and CA-weighted size distributions seen for plates 1, 2, and 3. However, this represents a small fraction of the overall mass and is likely due to diffusional losses of iron oxide nanoparticles not associated with the larger CA particles.

Although laboratory animals are commonly used for aerosol deposition studies, rodents such as the rabbit have a different lung morphometry than humans. In humans the airways branch dichotomously, meaning each parent airway divides into two equal sized daughter airways. The lung of the rabbit exhibits monopodial branching where multiple smaller daughter airways can branch off a single, longer parent airway [42]. In dichotomous branching, the distance a particle must travel from the trachea to the alveoli is similar for all the lobes whereas these distances can vary significantly in monopodial branching. The shortest distances occur in the upper lobes, which can result in these lobes experiencing higher concentrations of inhaled material for longer periods of time [43]. Thus, in the upper lobes, particles have a longer exposure time, increasing deposition by settling due to gravity; this mechanism likely dominates the probability of deposition over interception. Therefore, it is possible this would result in a minimal effect observed from alignment of the HARPs in the upper region of the lung.

This hypothesis is further supported by the higher total iron concentrations in the apical region of the lung compared with the middle and basal regions. This is seen in Figure 11 where the ratios of middle/apex and base/apex for the right and left lungs are all less than one for the untargeted rabbits. Despite the decreased efficiency of targeting in the apex, the effect of targeting is seen in the middle and basal regions of the lung where interception is expected to have a larger impact on the probability of deposition. In the apical region, iron concentrations were decreased with the application of the magnetic field. The method used to divide the lungs into three regions was rather crude and may have resulted in some of the conducting airways of the apex being incorrectly classified as part of the middle region. Targeting is expected to increase deposition in these incorrectly classified conducting apical airways, decreasing the total aerosol that would continue for possible deposition into the apically classified region. This would result in a perceived decrease in deposition in the apical region. A more detailed and accurate method of separating the regions of the lung, similar to the computer models of lung morphology used in conjunction with single photon emission computed tomography (SPECT) images by Schroeter *et al* [44], would provide valuable data regarding regional deposition.

It is important to note that these results were not statistically significant ($P > 0.05$). For example, when performing an unpaired two-tailed student's T-Test for independent samples on the data from Figure 11, the P values were found to be 0.98 and 0.55 in the middle and basal regions of the untargeted left lung respectively. In the middle and basal regions of the targeted right lung, these P values were found to decrease to 0.33 and 0.18 respectively. Statistical significance could potentially be obtained by increasing the number of subjects. However, a more desirable solution would be to decrease

variability in the experimental methodology by eliminating some of the limitations present in this study.

A number of these limitations are as follows.

Within the study group, consisting of 19 subjects, considerable inter-subject variability existed. This variability, in conjunction with the small number of subjects, led to results which were not statistically significant, although the data shows promise. Specifically, the baseline relaxation time ($T_{1,0}$) determined from the three baseline rabbits varied from 1249 to 1444 ms. This value, representing the properties of the lung tissue without the presence of iron, is critical in determining the iron concentration of the lungs in the exposed rabbits and our use of an average baseline relaxation time, rather than subject specific times, limits the discriminating power of the present study. Specifically, iron concentrations were determined from variation in T_1 times only as averages for each group; mapping of iron concentrations in individual rabbits would be possible only with individual $T_{1,0}$ baselines values.

Another source of unwanted variability occurs in the ventilation of the rabbits. Throughout the experiment, the blood-gas levels of the rabbits were taken to ensure proper ventilation and to determine if adjustments were needed. From this data it was found that 6 of the rabbits experienced hyperventilation and 5 experienced hypoventilation. However, there was no correlation found between abnormal breathing and the iron concentration distribution in the lungs of the rabbits.

Additionally, the ventilator used in this study did not measure the inhalation tidal volumes, eliminating the possibility of determining the total deposition fraction. If the majority of the aerosol entering the respiratory system deposits without the presence of

a magnetic field, any further increase in deposition with the application of a magnetic field is limited. The results of this limitation would be a decrease in observed effectiveness of the targeting.

In moving forward with this study, the limitations of inter-subject variability could be overcome by increasing the number of subjects, obtaining individual baselines for each subject, or increasing the effectiveness of the targeting. By measuring the individual baseline relaxation time ($T_{1,0}$) for each subject, a much more accurate estimate of iron concentration would be calculated in each animal. This would require an MRI scan to be taken of each subject before and after aerosol exposure, which would allow each rabbit to be its own baseline. Increasing the effectiveness of the targeting through optimization of the HARPs could further help in overcoming inter-subject variability. The probability of deposition with the application of the magnetic field will be increased by increasing the length of the HARPs. Alignment of longer particles with an external magnetic field would further increase interception with the airway walls [10].

3.5 Conclusion

This pilot study showed an increase in deposition of high aspect ratio particles (HARPs) of cromoglycic acid (CA) loaded with iron oxide nanoparticles with the application of a magnetic field in the middle and basal regions of the lung. As interception is not the dominant mechanism of particle deposition in the apex of rabbits, minimal effect was seen in the apical region. Further work must be done to decrease the effect of the inter-subject variability through the use of individual baseline relaxation times ($T_{1,0}$) and optimized HARP lengths to yield results that will be statistically significant. With further optimization of this technique it may be an effective method for the treatment of

diseases such as lung cancer by increasing the dose of drug delivered to a specific site within the lung.

4 Feasibility of optimizing HARP length for targeted drug delivery

4.1 Introduction

Both *in vitro* and *in vivo* work, discussed above, has shown alignment of iron oxide loaded HARPs to be a promising method of locally targeting drug delivery [10]. However, as seen in the *in vivo* study, there is room for improvement with this method of targeting. By optimizing this technique, a greater portion of the drug could be delivered to the site of interest. Improving the efficiency of the targeting, the exposure of unaffected tissue can be further decreased while simultaneously increasing drug concentrations where desired.

One method of increasing the efficiency of deposition with the application of a magnetic field would be to increase the strength of the magnetic field applied. The current strength of magnetic field is sufficient to overcome the aerodynamic torque exerted on the HARPs, so this increase would not increase the deposition of the particles due to interception [11]. In effect, this would increase deposition in the same manner as the study performed by Dames *et al* [7]. However, generating a magnetic field with enough strength to influence the deposition of these particles within the lung remains difficult, as previously discussed.

Alternatively, optimizing the size of the HARPs delivered could also be used to increase the efficiency of magnetic targeting. By increasing the length of the particles, deposition efficiency can be increased. As discussed previously, the primary mechanism of deposition being altered through creating a random orientation with the application of a magnetic field, as opposed to a parallel orientation, is interception. Interception of

these HARPs increases with increasing particle length [37]. By creating longer HARPs, the increase in deposition with the application of a magnetic field can be further increased. This is seen below in Figure 12 where deposition probability increases for randomly oriented particles with increasing particle length [45].

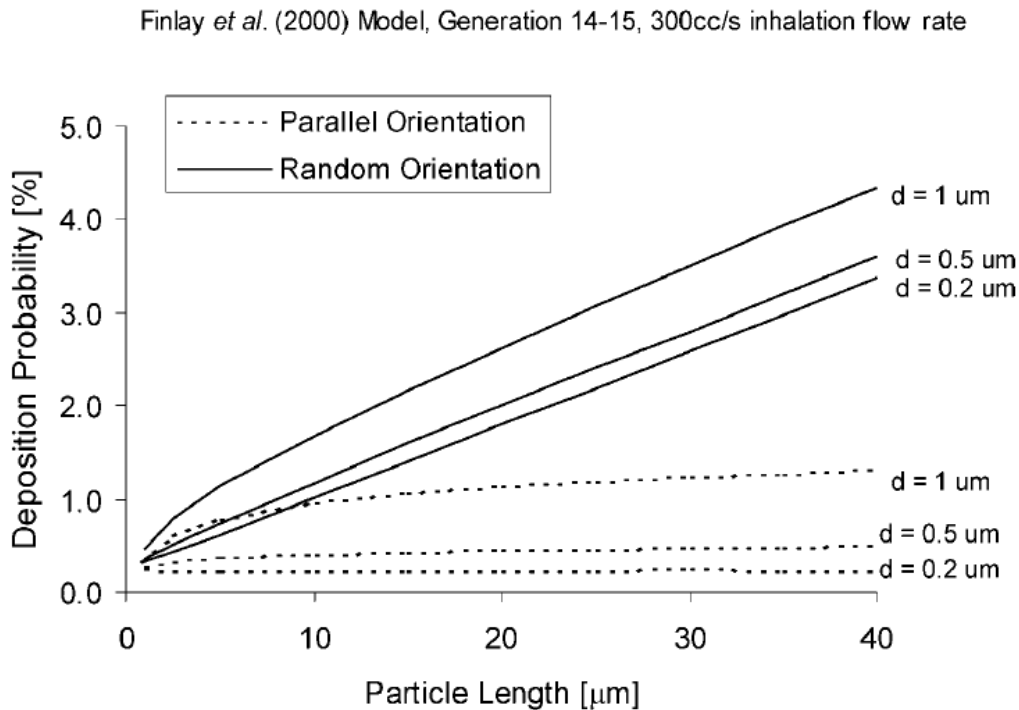


Figure 12: Deposition probabilities for HARPs of varying length and diameter in an airway bifurcation representing the branching between lung generations 14 and 15

In this study the feasibility of creating longer HARPs for targeted drug delivery was explored. Cromoglycic acid (CA) was used, the same drug used in the *in vivo* study. The length of these particles was limited not by the drug itself, but by the size of nebulized water droplets in which they were suspended. For this study, the focus was on creating larger water droplets, allowing for longer HARPs to be created. To create these larger droplets, an ultrasonic nozzle was selected. The droplets were then dried in a large evaporation chamber. The aerosol was then collected for both optical microscope and

scanning electron microscope (SEM) imaging. The influence of flow rate, relative humidity (RH), CA concentrations, and nozzle induced turbulence on the drying efficiency and final particle morphology were investigated.

4.2 Experimental Methods

4.2.1 Preparation of Ultrasonic Nozzle Suspensions

HARPs of cromoglycic acid (CA) were prepared following the crystallization method of Chan and Gonda [39] using cromolyn sodium salt purchased from Sigma-Aldrich Canada (Oakville, ON). Concentrations of 6, 2, 0.5, and 0.1 mg/ml of CA suspended in deionized water were used. Prior to being nebulized, the CA was resuspended in the deionized water by manual oscillation.

4.2.2 Aerosol Generation

Previously, Martin *et al* studied the effect of alignment in an airway bifurcation with the application of a magnetic field. In this study, the VMD and VML of the CA aerosol, created through nebulization of an aqueous solution of CA, were found to be 0.34 ± 0.02 μm and 2.0 ± 0.4 μm respectively. With the addition of magnetite to the aqueous solution the VMD and VML increased slightly to 0.47 ± 0.05 μm and 3.0 ± 0.5 μm respectively. The solution had a CA concentration of 2 mg per ml of deionized water. This solution was nebulized using the Hudson Updraft II jet nebulizer (Hudson Respirator Care, Inc., Temecula, CA). The Hudson nebulizer has been shown to create droplets with a mass median aerodynamic diameter (MMAD) of 4.2 μm [46]. From viewing much longer HARPs in the CA solution prior to nebulization, it is believed the MMAD of the droplets is the limiting factor on the VML of the HARPs created. To increase the length of the HARPs, an MMAD of approximately an order of magnitude larger was desired.

In an effort to maintain the same diameter of the HARPs while increasing the length, a similar method of nebulizing an aqueous solution was sought. Most nebulizers for pharmaceutical purposes have droplet diameters smaller than that desired here, as

larger droplets or particles closer to the size desired would largely deposit in the extra-thoracic region [1]. An ultrasonic nozzle was chosen as it could create the size of droplets desired at a relatively low flow rate. The ultrasonic nozzle creates droplets by vibrating a thin layer of liquid at an ultrasonic frequency perpendicular to the surface, creating waves on the surface which eject droplets as they reach a critical size [47]. The size of droplets is dependent on the frequency, with the droplet diameter being inversely proportional to the frequency.

A 60 kHz Ultrasonic Atomizing Nozzle (Sono-tek, Milton, NY, USA) was chosen and used in conjunction with a Broad Band Ultrasonic Generator (Sono-tek, Milton, NY, USA). Seen below in Figure 13 are the manufacturer provided droplet sizes for various frequencies. The mass mean diameter (MMD) of droplets expected to be created was approximately 50 μm for the 60 kHz model. The liquid was delivered to the nozzle through a Gear Pump (Sono-tek, Milton, NY, USA) with a variable flow rate from 20 to 70 ml/min.

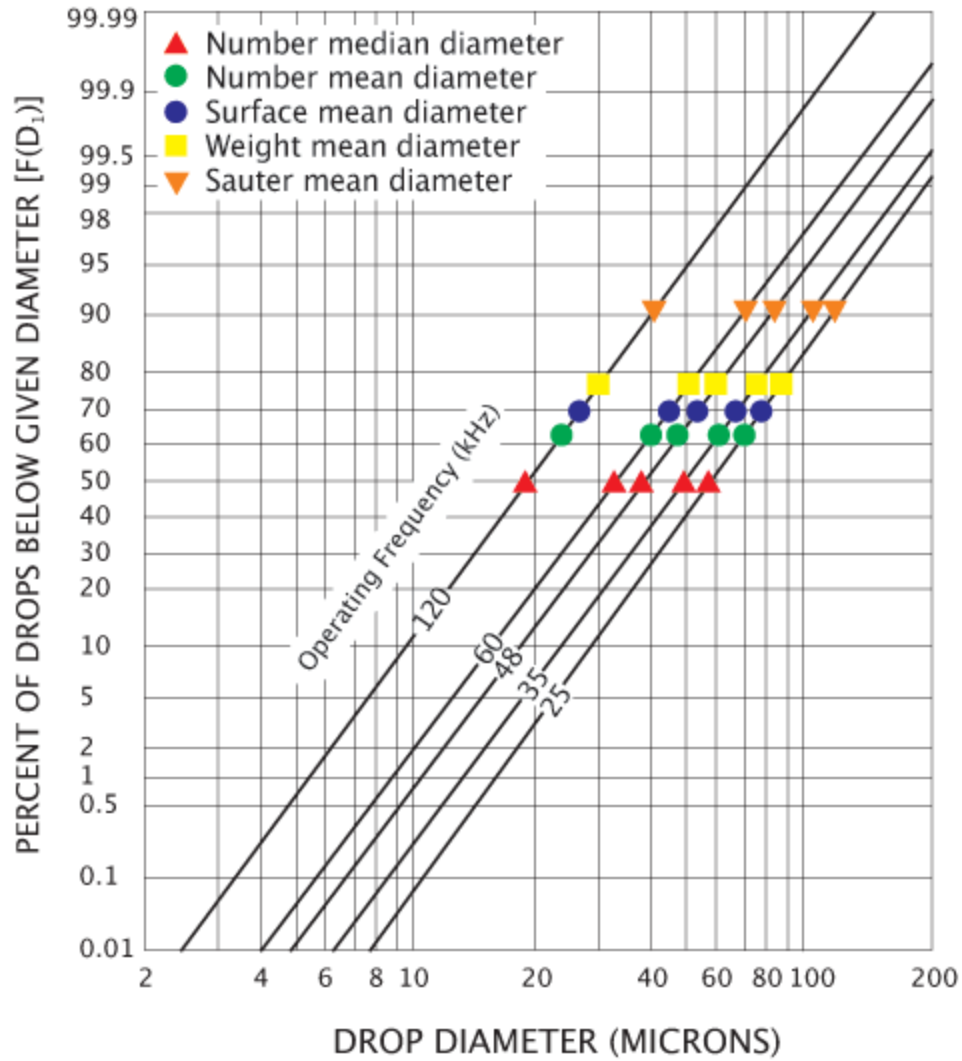


Figure 13: Droplet diameters for various ultrasonic nozzle operating frequencies (Sono-tek, Milton, NY, USA)

A schematic of the ultrasonic nozzle system can be seen below in Figure 14. Because the flow rate required for the ultrasonic nozzle was considerably higher than the nebulizer used previously, the nozzle was pulsed for a short period of time as opposed to running continuously. To accommodate for this, a switch was installed to allow for the pump to deliver fluid to the nozzle only when necessary. When the ultrasonic nozzle was turned off, the gear pump output to the reservoir. When the nozzle was

switched on for a short pulse, the pump output to the nozzle where the aerosol was generated.

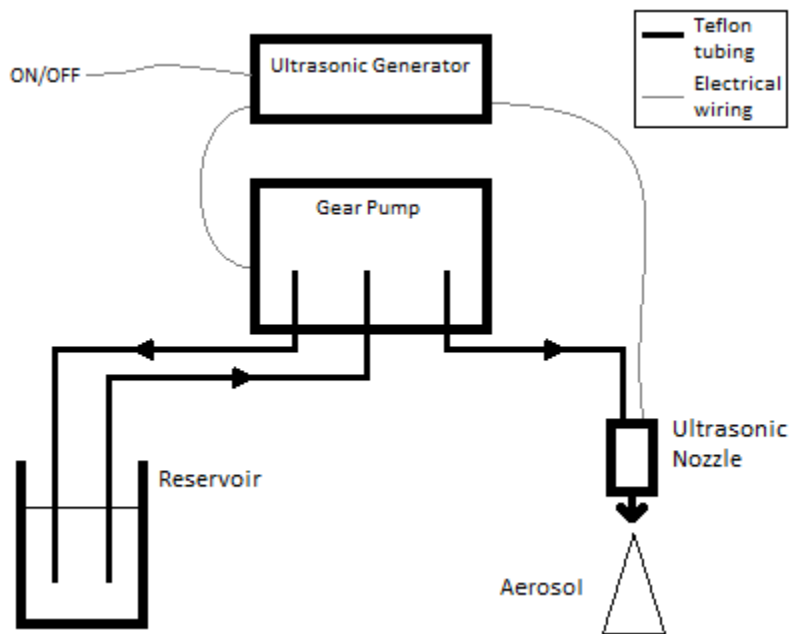


Figure 14: Schematic of Ultrasonic Nozzle System

The nozzle was calibrated as per the manufacturer's specifications. The optimal input power from the ultrasonic generator to the ultrasonic nozzle was determined by decreasing the power until the nozzle stalled and ceased atomizing the liquid. The optimal power was found by then increasing by 1 Watt. The optimal voltage for a flow rate of 20 ml/min was found to 2.6 Watts.

4.2.3 Drying of droplets

The HARPs of CA were initially suspended in an aqueous solution prior to nebulization. After exiting the ultrasonic nozzle they were then suspended in large water droplets. For these HARPs to exhibit the properties of aligning parallel to the walls of the airway, and ultimately aligning to an external magnetic field, they needed to be completely dry. In previous work, with the use of the Hudson Updraft II jet nebulizer (Hudson Respirator

Care, Inc., Temecula, CA), the droplet sizes were an order of magnitude smaller than those created with the ultrasonic nebulizer. More attention to the drying process was required to ensure these much larger droplets were dried fully.

4.2.3.1 *Settling Velocity*

As discussed in the background, aerosols will settle under the force of gravity at a terminal settling velocity. This is achieved when the drag force on a particle or droplet is equal to the force of gravity on the particle or droplet. Using the properties of water, as the quantity of CA present in the droplets was small, the settling velocities of water droplets with diameters ranging from 1 to 100 μm were plotted below in Figure 15. A droplet of 50 μm , the expected MMD of aerosol output from the ultrasonic nozzle, had a predicted settling velocity of approximately 75 mm/s.

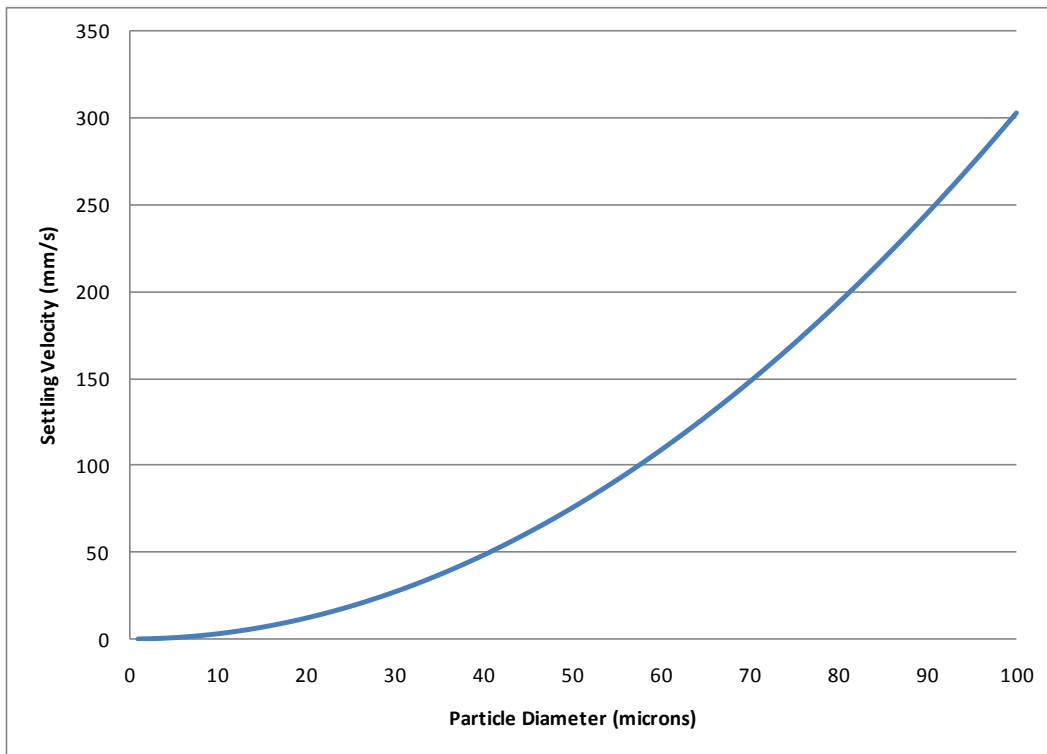


Figure 15: Settling velocities calculated for water droplets with diameters from 1 to 100 microns

When designing the evaporation chamber, it was important that the droplets not settle and deposit on walls or the collection filter prior to being dried. It is important to note however, that as the droplets were settling they were also evaporating. This meant that the size of the droplets was decreasing as they settled and thus their settling velocities were also decreasing. Knowledge of the rate of evaporation was required to further refine the design of an evaporation chamber.

4.2.3.2 Evaporation Rates

The evaporation rates (dd_p/dt), and in turn the droplet lifetimes (t_L), were important factors to consider when designing the evaporation chamber. It was important to ensure that the droplets were fully dried, leaving only HARPs of CA. As a droplet decreases in size and its diameter (d_p) decreases, its evaporation rate increases. The evaporation rate is defined as [22]:

$$\frac{dd_p}{dt} = \frac{4D_v M}{R\rho_p d_p} \left(\frac{P_d}{T_d} - \frac{P_\infty}{T_\infty} \right) \Phi \quad (7)$$

Where R is the universal gas constant, D_v is the diffusion coefficient of water vapour, P_d and T_d are the partial pressure and temperature of water vapour at the droplet surface, P_∞ and T_∞ are the partial pressure and temperature of water vapour at the ambient conditions, and Φ is the Fuch's correction factor.

Fuch's correction factor must be applied when the radii of the droplets approaches the mean free path of the molecules in the gas surrounding the droplets. In this case, the continuum assumption no longer applies and molecules of droplet can more easily escape, increasing the evaporation rate. Since the size of the droplets being produced is relatively large, the Fuch's correction factor (Φ) was neglected.

Another way of expressing the evaporation rate is κ , the rate of change of the surface area of the droplet with respect to time.

$$\kappa = \frac{8\pi D_v M}{R\rho_p} \left(\frac{P_d}{T_d} - \frac{P_\infty}{T_\infty} \right) \Phi \quad (8)$$

The droplet lifetime is simply the time for a droplet to evaporate completely. The droplet lifetime can then be determined by integrating the evaporation rate formula from d_p to zero. This results in the formula below [22]:

$$t_L = \frac{R\rho_p d_p^2}{8D_v M \left(\frac{P_d}{T_d} - \frac{P_\infty}{T_\infty} \right)} \quad (9)$$

The droplet lifetimes for diameters ranging from 1 to 100 μm for both dry air and air with a relative humidity (RH) of 35% were plotted below in Figure 16. The relative humidity influences the partial pressure and temperature terms in the equation for droplet lifetime. For the expected droplet size of 50 μm drying time of 1.6 seconds was expected for dry air, while for a RH of 35% that time almost doubled to 2.9 seconds. The effect of RH on the droplet lifetime for a 50 μm droplet of water can be seen below in Figure 17. With a relative humidity of over 75% the drying time begins to increase dramatically. With a relative humidity of 99% the drying time increased to 475 seconds. With a settling velocity for a 50 μm droplet of 75 mm/s, this would mean the droplet would require a dropping distance of 35 m to dry entirely. Given the space available for this experiment, this was not an unattainable size for the evaporation chamber. By providing dry air, a distance of 2.4 mm was required. However, constantly providing a droplet with ambient air at 0% RH is unrealistic. As the droplet begins to evaporate, the air surrounding the droplet will quickly become saturated, and the local RH will rise.

This situation is worsened further when considering the realistic situation of a cloud of droplets released together from the ultrasonic nozzle. With a pulse time of 1 second, a flow rate of 20 ml/min, and an MMD of 50 μm , there would be approximately 5×10^6 droplets released together in a dense cloud. It was important to provide the best possible drying environment for the droplets, as the local relative humidity was difficult to control.

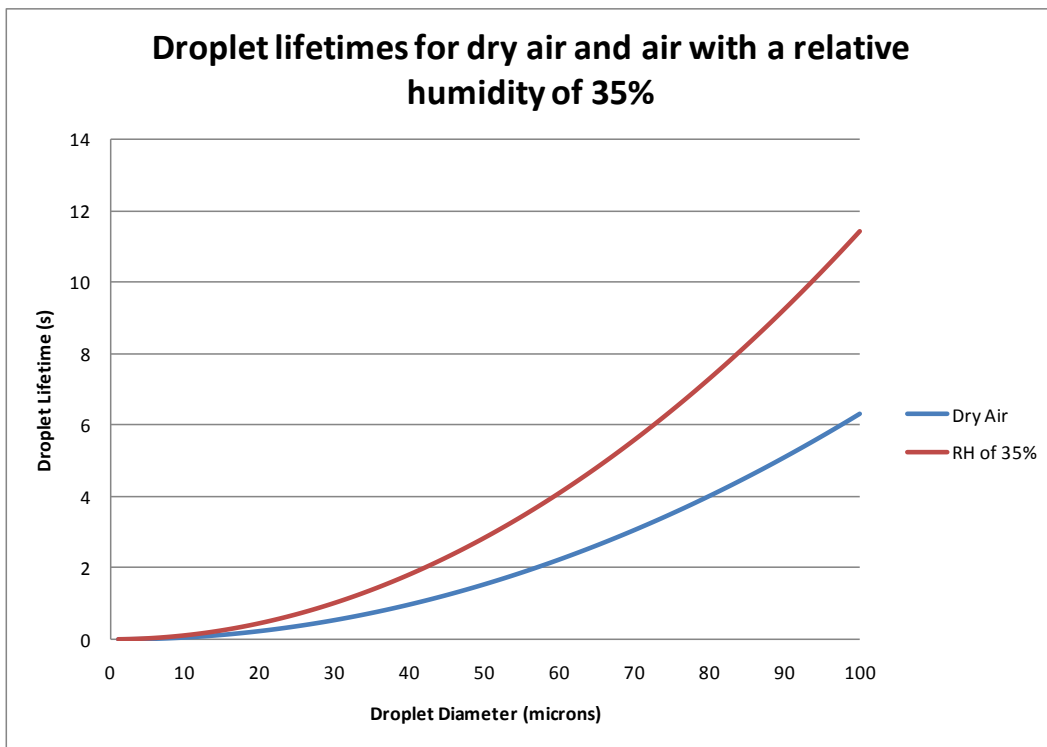


Figure 16: Droplet lifetimes for water droplets with diameters ranging from 1 to 100 microns for relative humidities of 0% and 35%

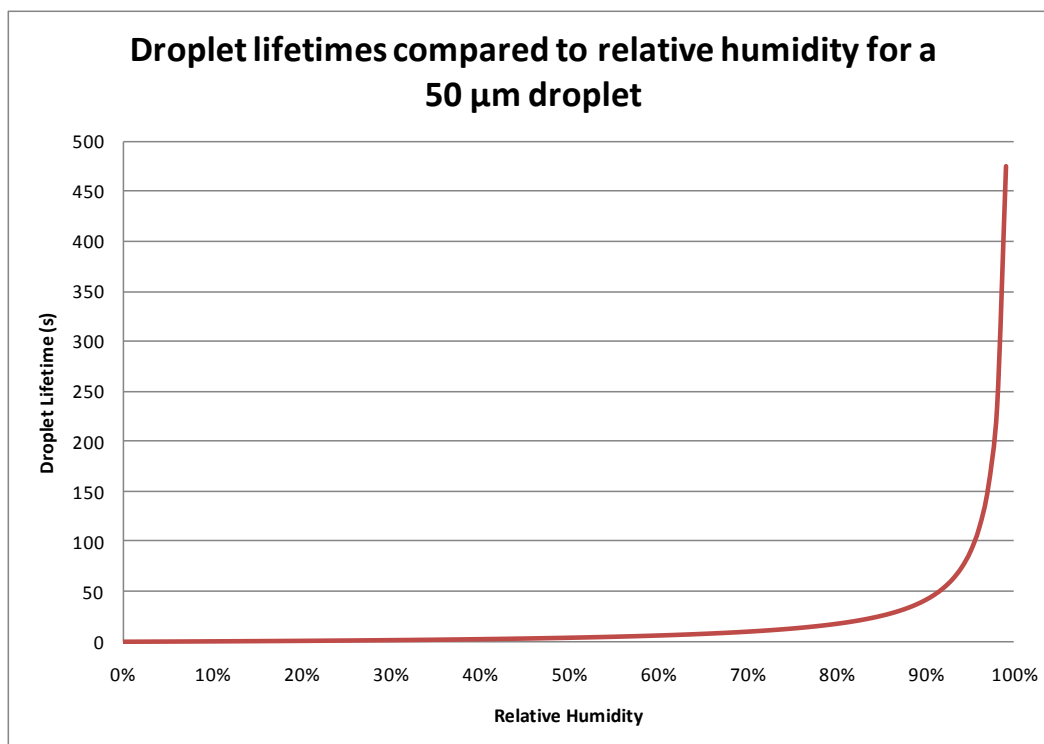


Figure 17: Droplet lifetimes for a 50 micron droplet of water at relative humidities ranging from 0% to 100%

4.2.3.3 Water Vapour Capacity of Air

Although the settling velocity and droplet lifetime were important considerations, ensuring there was enough dry air to make certain the air did not become saturated was also considered. One kilogram of air at 25°C and 1 atm has the capacity to hold up to 0.02 kg of water vapour [48]. With a 1 second pulse of the aqueous solution at 20 ml/min, a total of 0.33 g of water would be output from the ultrasonic nozzle. This would require 0.017 kg or approximately 14 l of dry air. This would require the chamber be at least 14 l. Given the length required to accommodate the high settling velocities and droplet lifetimes, it was expected this condition would be met.

4.2.3.4 Evaporation Chamber

Through consideration of the parameters explored above, in addition to some preliminary testing, an evaporation chamber was designed and constructed. The schematic of the chamber, including other equipment used can be seen below in Figure 18. Either ambient or compressed dry air was provided at the required flow rate into the top of the chamber where the CA aqueous solution was also delivered with a variable length pulse. At the bottom of the chamber were a filter or membrane for aerosol collection, a flow meter, and a vacuum pump.

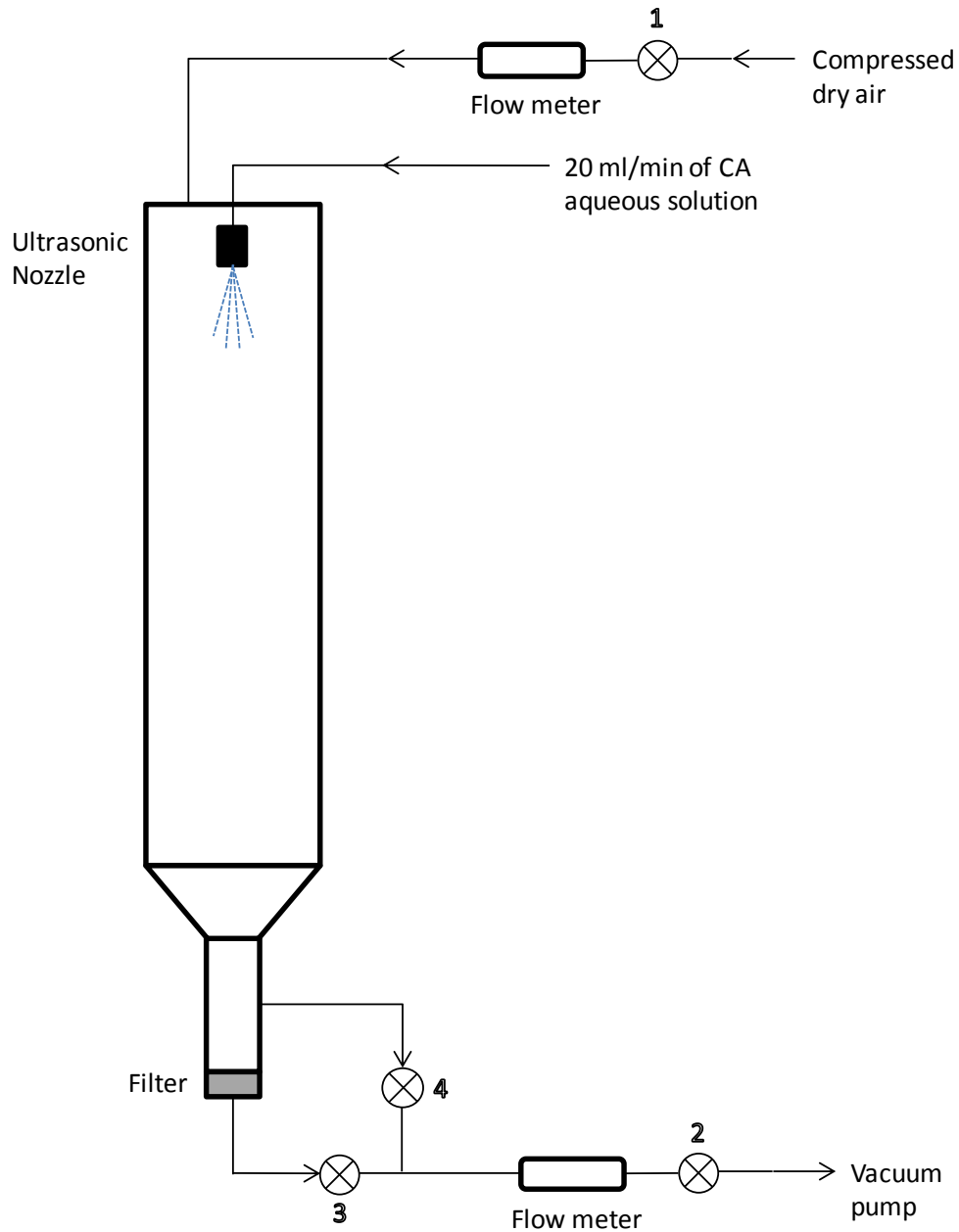


Figure 18: Experimental set-up of ultrasonic nozzle with evaporation chamber schematic

For this study, various flow rates of dry air were investigated ranging from 18 l/min to 0.2 l/min. For three flow rates in this range, the settling velocity of a 50 μm droplet was calculated and found to be significantly larger than the flow rate of the air inside the chamber. This can be seen below in Table 3 where residence times were predicted to be approximately 1 minute in all cases. However, it was expected that residence times

would be much larger than this, as mentioned previously, since as the droplets dry their size and thus settling velocity would be decreasing.

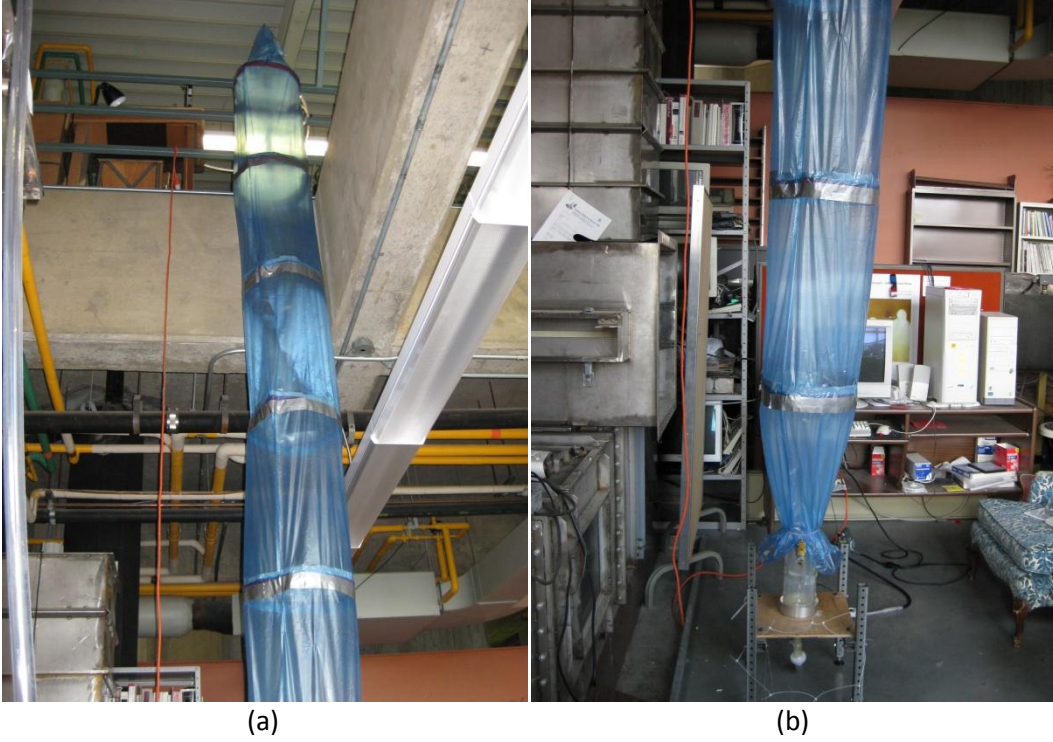
Table 3: Evaporation chamber residence times for a 50 micron droplet for flow rates of 18, 11, and 0.2 l/min

Flow rate [l/min]	Air Velocity in Chamber [mm/s]	Settling Velocity [mm/s]	Total Velocity [mm/s]	Residence Time [s]
18	0.0354	75	75.0354	61.5909
11	0.0216	75	75.0216	61.6022
0.2	0.0004	75	75.0004	61.6197

Prior to pulsing the ultrasonic nozzle, valves 1 and 2 in Figure 18 were adjusted to provide the desired flow rate. After each one second pulse the chamber was emptied for 30 minutes for all three flow rates to ensure most particles had been collected at the bottom. At this point, to empty the chamber of the now saturated air valve 3 was closed, valve 4 was opened and the flow rate was increased using valve 2 to 20 L/min. After this dry air exited above the filter for 10 minutes, valve 2 was adjusted to decrease the flow rate down back to the desired rate and valve 3 was then opened and valve 4 was closed.

The chamber was constructed from polyethylene plastic, mild steel wire, and adhesive tape. The diameter of the cylindrical chamber was approximately 0.4 m and the length was a total of approximately 5.0 m. It was suspended in a two-storey lab to allow for the long length of the evaporation chamber. Images of the evaporation chamber and where the nozzle and dry air were located can be seen below in Figure 19. In the cases where compressed dry air was used, the top portion of the chamber was not fully sealed, this allowed any small differences in input and output flow rates to be

compensated for with ambient air. In the case of ambient air, the top of the chamber was simply open. At the bottom of the chamber, an aluminum cylindrical tube and funnel were used to contract the flow for the collection of the samples and for attachment to the flow meter and vacuum pump.



(c)

Figure 19: Final evaporation chamber: (a) Top portion (b) Bottom portion (c) Input of compressed dry air and ultrasonic nozzle

4.2.4 Orifice Design

Although it was the simplest solution to increase the droplet size to yield longer HARPs that would not be possible in smaller droplets, there were additional complications associated with this choice. The goal of creating longer HARPs was to have single particles separated from each other that would behave with specific characteristics within the lung. To accomplish this, by simply evaporating the water, it was required that there be only one HARP per droplet. However, if maintaining the same concentration of CA in the previously used aqueous solution, increasing the diameter of the droplet by one order of magnitude would result in increasing the total number of particles in the droplet by three orders of magnitude. The number of particles per droplet is directly related to the droplet volume and the concentration. In the present case, with spherical droplets, the volume is related to the particle diameter cubed. Having 1000 particles in a droplet would likely result in large clusters of HARPs which would not behave with the same aerodynamic properties as individual HARPs.

One alternative was to decrease the concentration of the CA in the aqueous solution. This was possible, but only to a certain extent. Previously, Martin and Finlay [10] used concentrations of 2 mg/ml. CA is not soluble in water at this concentration, however decreasing the concentration has a limit where the CA begins to dissolve in the deionized water. The CA is soluble at a concentration of 0.21 mg/ml of deionized water [49]. In addition to the issues of solubility, lowering the concentration also lowered the total mass of CA available, making collection of a large enough mass of CA for sampling difficult.

An alternative is to instead use turbulence to deaggregate these clusters of HARPs. The turbulent flow field has eddies spanning a range of sizes, which would essentially rip apart the cluster of HARPs, and create individual aerosolized HARPs. This can be achieved by reducing the cross-sectional area of the flow, thus increasing the fluid velocity. A reduction of the cross-sectional area was easily achieved with the addition of a small aluminum plate with three very small cylindrical orifices. This was placed directly above the 0.2 μm pore polycarbonate membrane (Isopore GTTP04700; Millipore, Billerica, MA) for sample collection. To select an ideal size of orifice, the turbulent scales of the turbulent flow field were investigated.

Following the method of Finlay [1] the turbulent scales were calculated. The largest eddies, the ones containing the most energy, are defined by the integral scales: velocity [u_i], length [l], and time [t_i]. The smallest eddies are defined by the Kolmogorov scales: velocity [v_k], length [η], and time [t_k]. The Kolmogorov scales can then be related to the integral scales [50] using:

$$\frac{n}{l} \approx \left(\frac{u_i l}{\nu} \right)^{-3/4} \quad (10)$$

$$\frac{t_k}{t_i} \approx \left(\frac{u_i l}{\nu} \right)^{-3/4} \quad (11)$$

$$\frac{v_k}{u_i} \approx \left(\frac{u_i l}{\nu} \right)^{-1/4} \quad (12)$$

Where ν is the kinematic viscosity. For the round orifice created, with an $x/D > 20$ (where x is the distance from the exit of the orifice and D is the orifice diameter), the length scales can be approximated from experimental data [50,51] as:

$$\frac{u_i}{U_{\max}} \approx 0.3 \quad (13)$$

$$\frac{l}{x} \approx 0.06 \quad (14)$$

$$U_{\max} \approx 0.06U_{\text{nozzle}} \frac{D}{x} \quad (15)$$

Using this information, a thin plate with three orifices of 1 mm each was chosen to be used at 16 l/min. The resulting integral and Kolmogorov scales can be seen below in Table 4. A value of x of 0.02 m was chosen as it reflected the distance from the nozzle to the filter in addition to satisfying the $x/D > 20$ condition stated earlier. The Mach number was calculated to ensure there were no compressible flow effects. Here, the Kolmogorov length scale was found to be approximately 7 μm .

Table 4: Results for integral and Kolmogorov turbulence scales for orifice

D	0.001	m
Q	5.33	L/min
	8.89E-05	m ³ /s
x	0.02	m
l	0.0012	m
U_{nozzle}	113.18	m/s
Ma	0.33	
U_{max}	37.35	m/s
u_i	11.20	m/s
t_i	1.07E-04	s
v	1.50E-05	m ² /s
Re_i	896.36	
η	7.33E-06	m
t_k	6.54E-07	s
v_k	2.05	m/s

4.2.5 Sample Collection and Imaging

4.2.5.1 Sizing of individual HARPs

For the collection of the aerosol for the sizing of the individual HARPs, it was desirable to first collect the sample on a filter and then resuspend the CA in water for the purposes of dilution. This was necessary so that the HARPs would be dispersed enough so that individual particles could be identified and measured.

Since the HARPs would be resuspended in deionized water, it was not necessary to ensure the droplets were fully dried. Ambient air was entrained at 0.2 L/min into the top of the evaporation chamber. The ultrasonic nozzle, loaded with an aqueous solution of 6 mg/ml of CA in deionized water, was pulsed for 3 seconds. At the bottom of the chamber was a bacterial air filter (Respirgard; Vital Signs, Inc., Totowa, NJ) which was cut in half to expose the surface of the filter and increase the surface area onto which the particles could fall. After the nozzle was pulsed for 3 seconds, the chamber was emptied for 30 minutes. The saturated air was then replaced with dry air for 10 minutes at a flow rate of 20 l/min. This was repeated 8 times. A summary of the conditions for the sizing experiment can be seen below in Table 5.

Table 5: Experimental settings for sizing experiment

CA concentration	Pulse length	Air flow rate	RH of air
[mg/ml]	[s]	[l/min]	
6	3	0.21	23.6%

The filter was then washed with 10 ml of deionized water to resuspend the HARPs of CA in an aqueous solution. This suspension was then used to create samples for

measurement in two different ways. Since the length of the particles was expected to be on the order of 10 μm , an optical microscope (Zeiss Axio Imager.A1; Carl Zeiss MicroImaging GmbH, Jena, Germany) was used to take images of slides prepared using the suspension of CA HARPs in deionized water. A sample of an optical microscope image can be seen below in Figure 20.

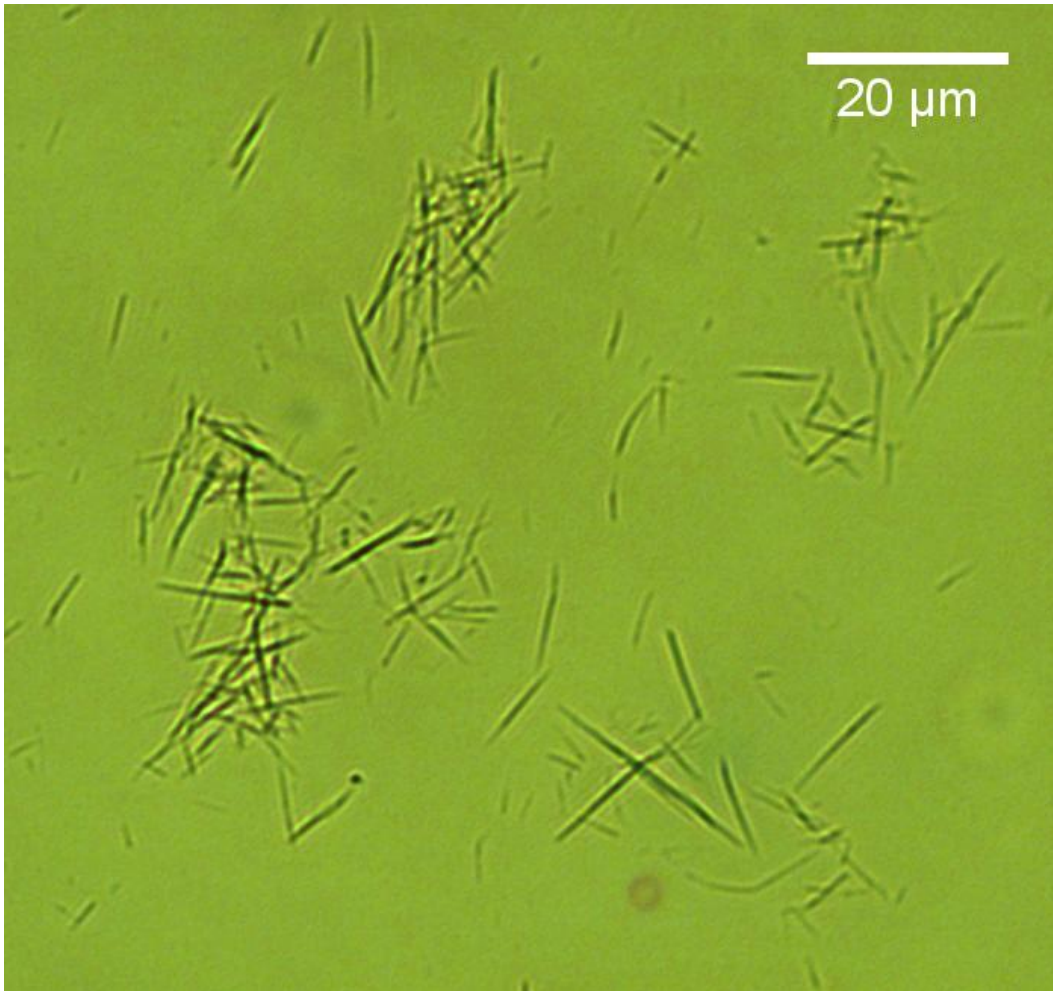


Figure 20: Sample of optical microscope image used for sizing length of individual HARPs

The diameters of these particles were expected to be on the order of 0.5 μm which required a much higher magnification scanning electron microscope (SEM) analysis. SEM samples were prepared by first attaching two-sided carbon adhesive tabs to SEM stubs, and then attaching a small square cut from a 0.2 μm pore polycarbonate

membrane (Isopore GTTP04700; Millipore, Billerica, MA). The stub was then rotated in a Dremel drill (Minimite 4.8V Model 750; Dremel, Racine, WI) to spread out the suspension over the entire sample surface area while 1.5 and 2.5 μl drops of the aqueous solution were dropped onto the polycarbonate membrane. The stubs were sputter coated with gold prior to analysis. SEM (5-2500; Hitachi, Japan) images were then taken at magnifications of 3000x and 10000x. A sample of one of these images can be seen below in Figure 21.

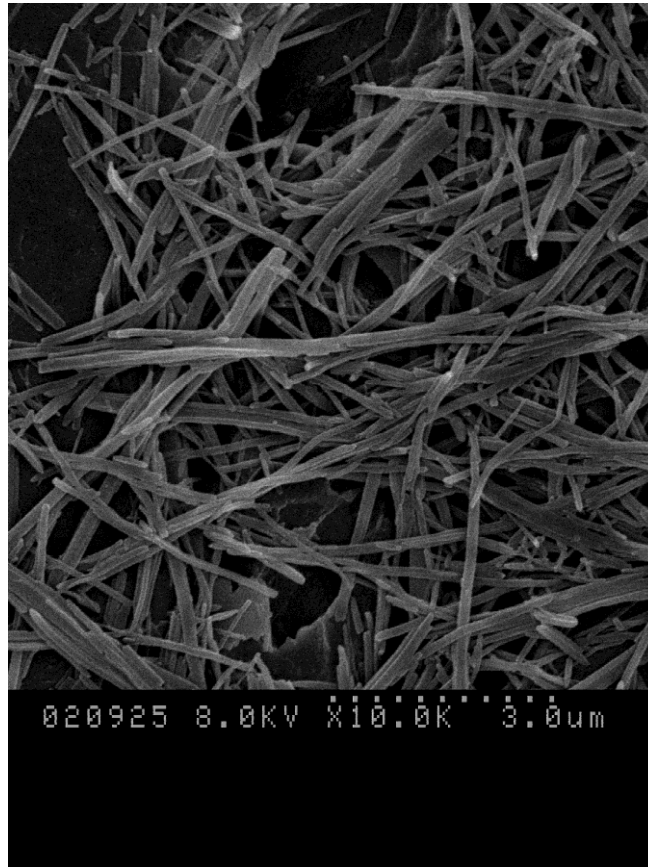


Figure 21: Sample of scanning electron microscope (SEM) image of HARPs for measurement of diameters at 10000x magnification

The lengths of these HARPs were measured using rules similar to those of Platek *et al* [52]. Only HARPs that were completely visible on the slide were counted. In addition, any HARP in a cluster with only one of the ends visible was not counted. When HARPs

were curved, their length was measured from tip to tip. The diameters were measured as the thickest point perpendicular to the edge of the HARP. Again, if a particle was concealed, or not fully visible in the field of view, it was not counted. After a particle was measured, it was marked to ensure no particle was measured more than once.

4.2.5.2 Particle morphology collection and imaging

As discussed above, the increase in droplet diameter will introduce more than one HARP per droplet. It was desirable to determine resulting structure of these clusters of HARPs. To study the size and morphology of the clusters created by the ultrasonic nozzle, a different approach was necessary. For the purposes of measurement, resuspending the CA in water was an ideal solution as it allowed for the HARPs to be dispersed. However, once resuspended, the structures resulting from numerous HARPs having been dried together in a single droplet would be lost. To compensate for this, a 0.2 μm pore polycarbonate membrane (Isopore GTTP04700; Millipore, Billerica, MA) was introduced at the bottom of the evaporation chamber which was then used to create samples for SEM analysis. Pieces of this membrane could then be analyzed directly, without the need for resuspending the HARPs.

SEM samples were prepared by first attaching two-sided carbon adhesive tabs to SEM stubs. Three small squares were then cut from the exposed 0.2 μm pore polycarbonate membrane (Isopore GTTP04700; Millipore, Billerica, MA) and attached to the stubs. The stubs were then sputter coated with gold prior to analysis. SEM (S-2500; Hitachi, Japan) images were then taken at magnifications ranging from 60x to 6000x. Nine tests were completed at various flow rates, pulse times, CA concentrations and relative humidities. An outline of these tests can be seen below in Table 6. After the

first three experiments at high relative humidities with longer pulse lengths, the parameters that could be controlled were optimized further to improve the drying capabilities of the evaporation chamber.

Table 6: Experimental settings for ultrasonic nozzle generated HARPs

CA concentration [mg/ml]	Pulse length [s]	Air flow rate [l/min]	RH of air
0.5	3	18.1	49.3%
0.5	3	10.9	50.3%
0.5	3	2.0	50.7%
0.5	1	14.7	dry air
0.5	1	7.4	dry air
0.5	1	1.0	dry air
2	1	15.0	dry air
2	1	7.5	dry air
2	1	1.0	dry air

4.3 Results and Discussion

4.3.1 Expected particle morphology

As discussed previously, the increase in the size of the diameter of the nebulized droplets resulted in an increase in the number of particles in each droplet. By increasing the diameter of the droplets by one order of magnitude, an increase in the number of particles per droplet of approximately 1000 times was expected from the study done by Martin and Finlay [10]. It was unclear what the final structure would be of a droplet dried containing a large number of HARPs.

Control of particle morphology for pharmaceuticals has been successfully achieved through spray drying [53]. Through control of drying rate and droplet and solute

properties, different morphologies can be created. In the case of milk powders, it was found that as the droplet dried, and the surface of the droplet receded, the concentration at the surface increased [54]. Specifically in the case of nanoparticles suspended in a solution, it was found that as the surface of the droplet receded, a shell of nanoparticles was created [55]. The rate of the surface of the droplet receding was greater than the rate of diffusion of the nanoparticles [55]. This ratio defined by the Peclet number (Pe), was used to help predict particle morphology. Here κ is the evaporation rate of the surface of the droplet and D is the diffusion rate of the solute in the solution.

$$Pe = \frac{\kappa}{8D} \quad (16)$$

The evaporation rate of the expected droplet diameter was previously defined in the evaporation chamber section. The Stokes-Einstein diffusion rate was defined as:

$$D = \frac{kT}{3\pi\mu d_p} \quad (17)$$

Where k is Boltzmann's constant, T is temperature, μ is viscosity of the solution and d_p is the diameter of the particle. This equation defines the diffusion coefficient for spherical particles, so it must be adjusted to accommodate for the shape of the HARPs suspended in the droplet. From Asgharian *et al* [56] an equivalent diffusion diameter of a HARP can be determined from the aspect ratio and HARP diameter. For a diameter of 0.1 μm and an aspect ratio of 60, the equivalent diffusion diameter was found to be approximately 0.9 μm . Using this, the Peclet number was calculated for relative humidities ranging from 0% to 100%. For $Pe \ll 1$, the rate of diffusion is high enough that as the surface of the droplet is drawn in, the suspended particles have time to diffuse towards the centre

of the droplet. If $Pe \gg 1$, the particles will not have time to diffuse in to the centre of the droplet and as the concentration of particles on the outside of the droplet increases, a shell will be formed. As seen below in Figure 22, the Pe for almost the entire range of relative humidities is much greater than 1. Even at 100% humidity, the Peclet number is 8.5. To develop a shell like structure from the drying process the Peclet number must be approximately 10. This indicates that for most of the possible drying scenarios present in the evaporation chamber, the HARPs suspended in the droplets are likely to create shells of CA as the droplet evaporates.

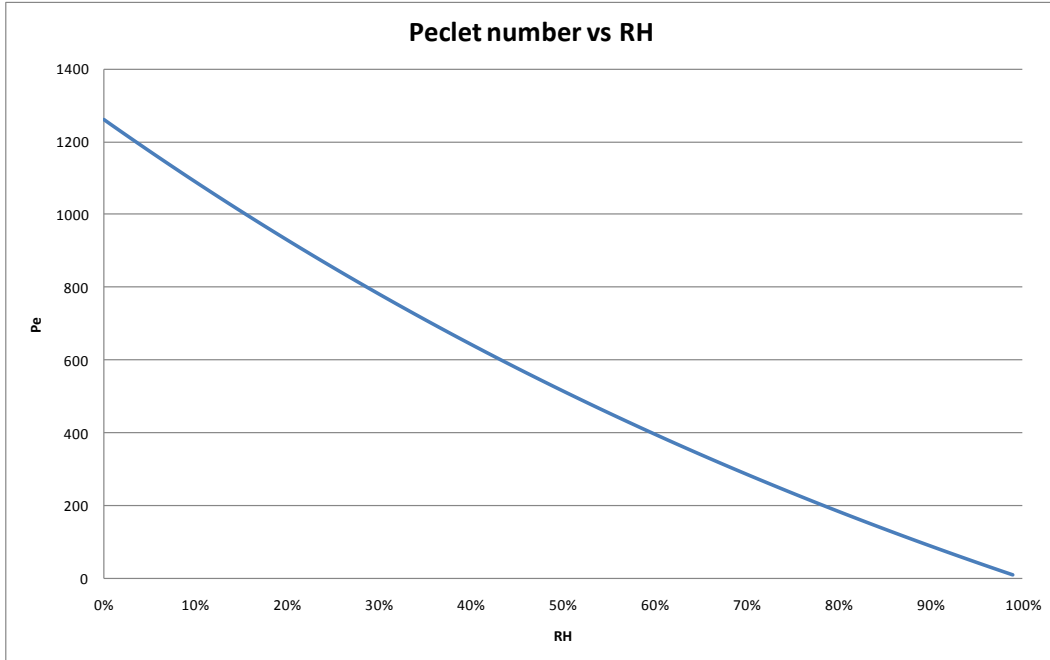


Figure 22: Peclet numbers for relative humidities ranging from 0% to 100%

4.3.2 Interpretation of SEM images to infer 3D particle morphology

The use of SEM analysis can provide valuable clues as to the shapes and structures of the clusters of HARPs created through nebulization with the ultrasonic nozzle. However, partly due to the collection method, and partly due to the limitations of 2D imaging,

they do not offer a full picture of the particle morphology. Because of the small diameter of the polycarbonate membranes used for the sample collection, there was a significant pressure difference on either side of this membrane. This would essentially cause the 3D particles to be collapsed down into 2D structures. In order to recognize the difference between a particle with a volumetrically uniform concentration of particles and a particle with a shell type structure, predictions of what the 2D structures would be were necessary. This is similar, although considerably simpler, to the analysis done on 2D images obtained from the Hubble telescope, where the images are analyzed to understand the 3D structures present [57].

4.3.2.1 Uniform distribution

If as the droplet dries the HARPs have time to diffuse away from the receding surface, a uniform distribution of particles within the droplet would be expected. If this particle was then collapsed into a 2D structure, the image seen from the SEM analysis would appear differently. It was desirable to know what the concentration distribution would be of particles collapsed into the 2D circle seen in the SEM. To simplify the analysis, a quarter of a circle was investigated. To determine the entire concentration distribution, this quarter circle would be revolved around 360° and doubled to add the bottom half of the sphere. Seen below in Figure 23 is a schematic of how a uniform particle distribution would appear in this slice of the droplet. As this circle collapses down on itself, onto the x-axis, the particles would pile on top one another. From this analogy, it can be seen from observation of that in the centre of the circle the greatest number of particles would be seen and thus the highest concentration, with a lower number of particles and concentration at the outer edge. This can be further refined, and when the

two hemispheres of the circle are added together, the concentration on the x-axis (C_x) is simply:

$$C_x = \frac{\sqrt{x^2 - r^2}}{2} \quad (18)$$

where x is the radial distance from the centre of the circle. This can be seen in Figure 24 for a droplet with a radius of 1. With this concentration distribution, the inner half of this slice of the circle would hold 60% of the total particles.

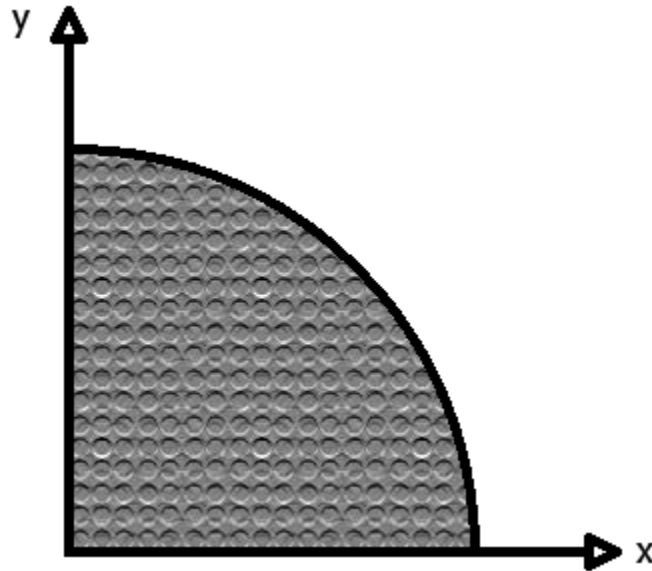


Figure 23: Schematic of a quarter circle slice from a droplet with a uniform distribution of particles

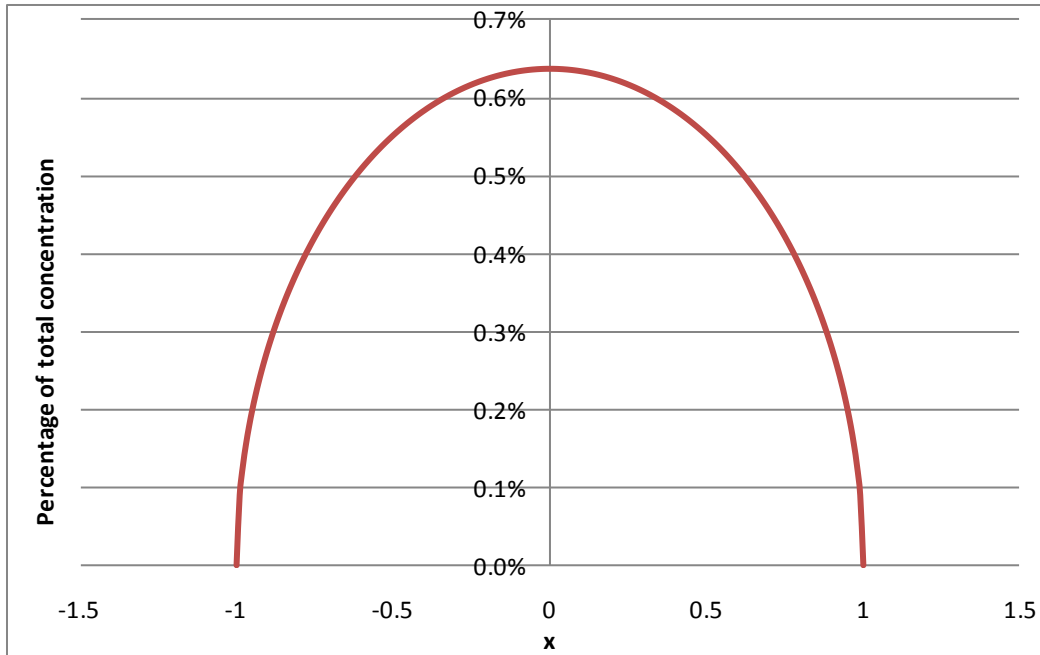


Figure 24: Concentration distribution for a collapsed spherical droplet with a uniform distribution of particles

4.3.2.2 Shell particle distribution

If the Peclet number is much greater than one, as predicted, the droplets containing numerous HARPs would dry to form a shell like structure. As in the case of uniform distribution, a quarter of a circle was investigated. In the case of a shell, the scenario was simplified to be particles equally spaced along the edge of the circle. As seen in Figure 25 the particles are equally spaced at a distance of dr . When envisioning this structure collapsing onto the x-axis, the variable of interest is dx . A smaller value of dx , having the particles more closely packed together, would correspond to a higher concentration. It can be observed from Figure 25 that as x increases, dx decreases, suggesting that concentrations for this morphology will be higher at the outer edge.

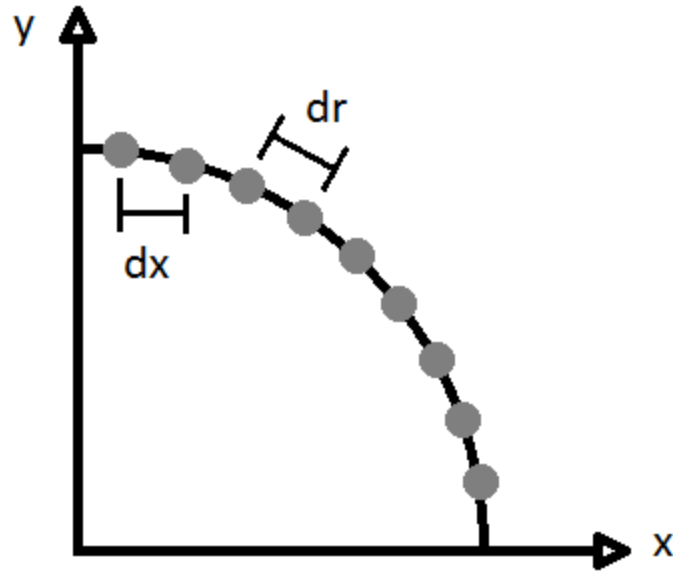


Figure 25: Schematic of a quarter circle slice of a shell-like concentration distribution

Knowing that $x = r\cos\theta$, dr is constant, and that the concentration is directly correlated to $1/dx$, the concentration is found to be:

$$C_x \propto \left| \frac{\csc\left(\arccos\left(\frac{x}{r}\right)\right)}{dr} \right| \quad (19)$$

Where C_x is the concentration and r and dr are constant. It is also important to note that at the point where $x = \pm r$ the equation predicts an infinite concentration. The concentration at these points was set to be zero, as just outside the radius of the shell there would be no particles. This is plotted in Figure 26 and it can be seen the opposite trend occurs from that of the uniform particle distribution. In this case approximately 65% of particles lie outside $x = \pm 0.5$. A 3D visualization of the concentration distribution for a quarter of a crushed shell can be seen in Figure 27. The vertical axis represents the concentration at that point on the 2D circle resulting from crushing the shell.

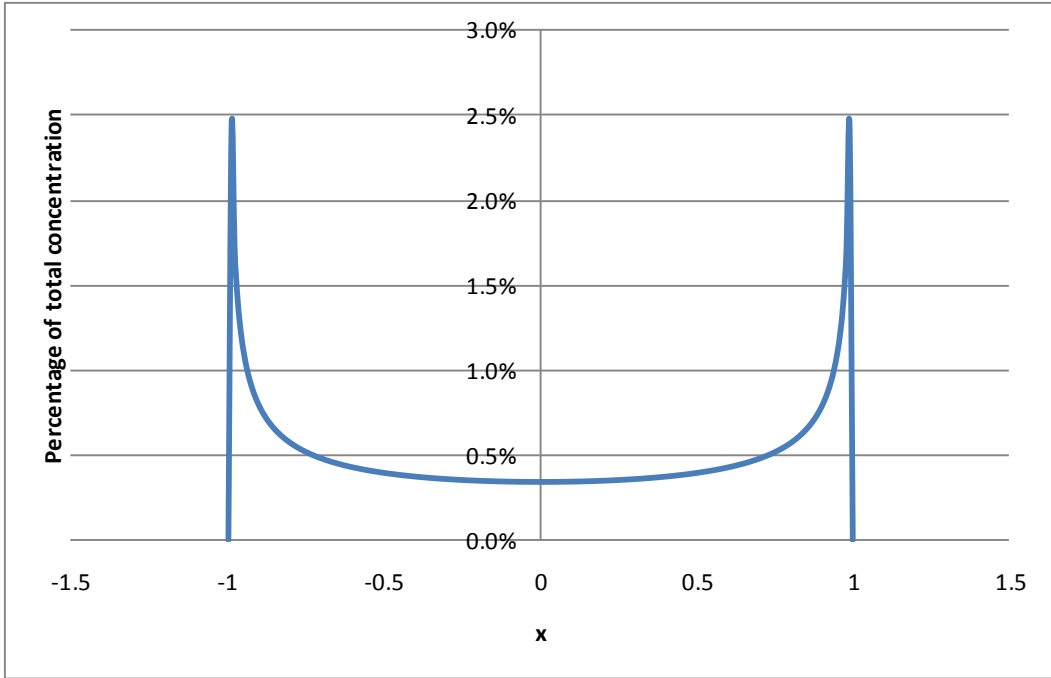


Figure 26: Concentration distribution for a collapsed spherical droplet with a shell-like structure

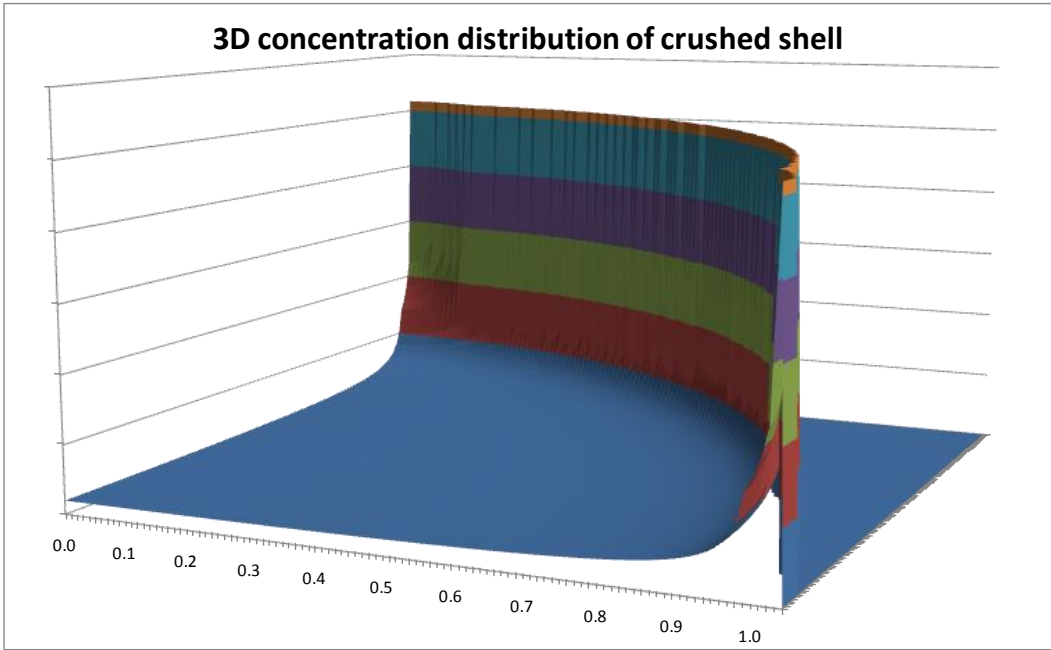


Figure 27: 3D Visualization of concentration distribution of a 2D circle resulting from a crushed spherical shell

This was then further refined to create a shell with three concentric layers of particles. This is more representative of the realistic case, where the shell-like structure is more

than one particle thick. In this case, the peaks would tilt slightly towards the centre and the peak at the outside would drop from approximately 2.5% to just over 1.5%.

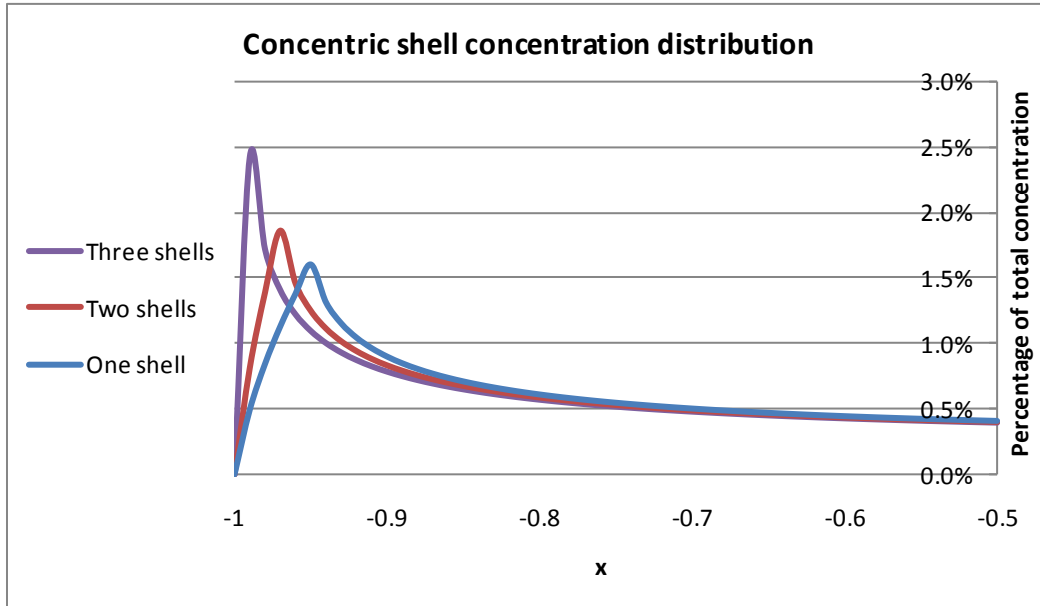
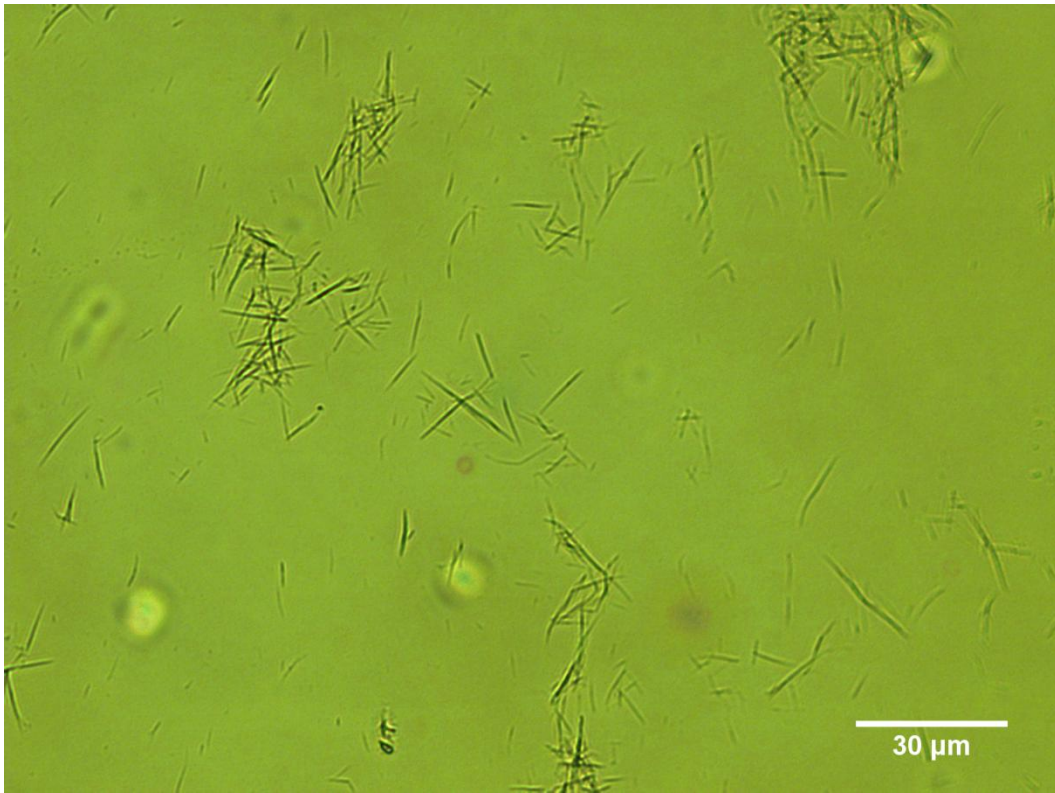


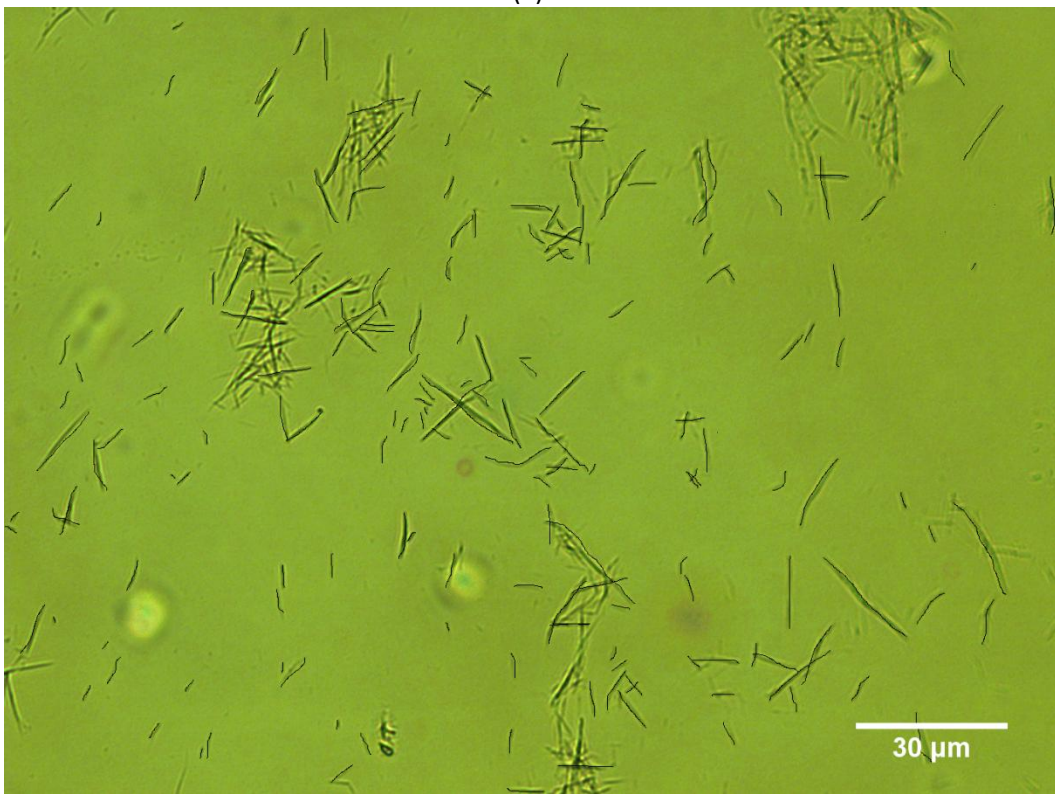
Figure 28: Concentration distribution for a collapsed spherical droplet with a shell-like structure of varying thicknesses

4.3.3 Sizing of individual CA HARPs

To create longer HARPs the ultrasonic nozzle was used due to its larger droplet size. It is thought the size of the droplet restricts the length of the particle suspended within the droplet [45]. The count median length (CML) and count median diameter (CMD) were found from analyzing both optical microscope and SEM images. Seen below in Figure 29 are optical microscope images used for determining the CML before and after sizing was completed. Once a particle was counted, it was marked out to ensure it was not counted twice.



(a)



(b)

Figure 29: Optical microscope images for determining the CML: (a) before measurement (b) after measurement and mark up

In total, 328 HARPs were measured to determine the CML and 155 HARPs were measured to determine the CMD. The CML was found to be $5.9 \pm 4.2 \mu\text{m}$ and the CMD was found to be $0.1 \pm 0.01 \mu\text{m}$. Additionally, the geometric standard deviation was calculated for both the length and the diameter. The sizing parameters are summarized below in Table 7.

Table 7: Sizing parameters for individual CA particles created

CA	
CML	$5.9 \pm 4.2 \mu\text{m}$
σ_L	1.86
N_L	328
CMD	$0.1 \pm 0.01 \mu\text{m}$
σ_D	1.4
N_D	155

The CML and CMD are expressed as \pm one standard deviation

Given the MMD of the droplets was $50 \mu\text{m}$, The CML found was lower than expected, however the high standard deviation associated with this term is of interest. Within the particles examined, there were particles as long as $23.6 \mu\text{m}$ found. It appears that although longer particles were being created, shorter particles were also being created. Because of the smaller particle diameter, the aspect ratio for these HARPs was found to be approximately 59. Martin and Finlay created HARPs with aspect ratios of approximately 6 [10].

4.3.4 Ultrasonic nozzle aerosol particle collection and imaging

4.3.4.1 Ambient Air

The first three experiments were done with ambient air at three different flow rates of: 18.1 l/min, 10.9 l/min, and 2.0 l/min. The ambient air for these experiments had a RH of

50.1%. A three second pulse of 0.5 mg/ml of CA was sprayed into the chamber and then emptied for 30 minutes at each flow rate. Seen below in Figure 30 is an SEM image taken from a sample generated with a flow rate of 18.1 l/min. It can be seen, that although these images show a definite increase in concentration at the edges, it is far greater than that predicted earlier. It is likely this ring type structure was formed as a wet droplet fell onto the polycarbonate membrane and spread out. Additionally, as the droplet dried, the same mechanism that would have caused a spherical shell, likely aided in creating this ring type structure as the droplet dried on the membrane. As the edge of the circle receded, the HARPs diffused at a much slower rate, resulting in an increase in concentration at the edge. The edge of the center droplet in Figure 30 can be seen in more detail in Figure 31.

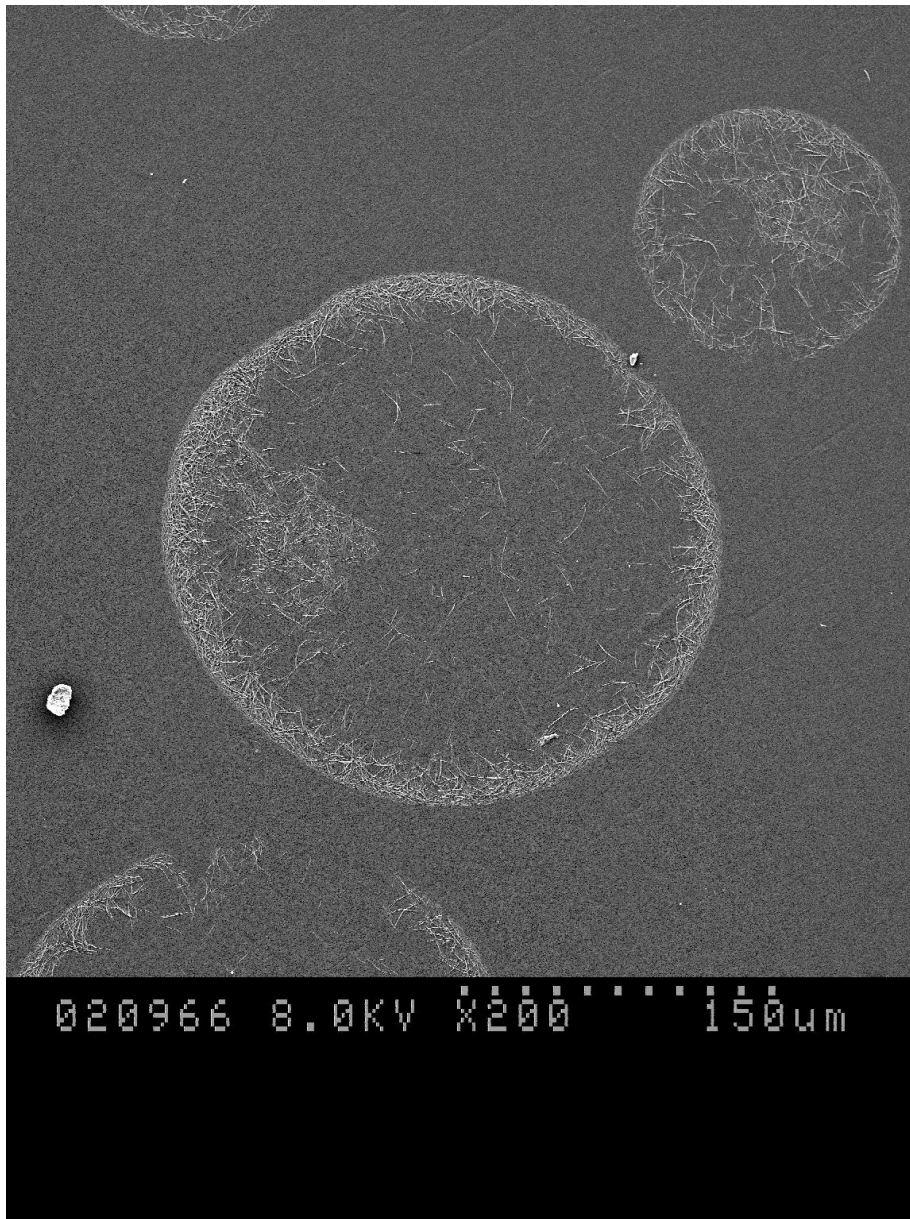


Figure 30: SEM image of particles generated with 0.5 mg/ml of CA and ambient air at 18.1 l/min at 200x magnification

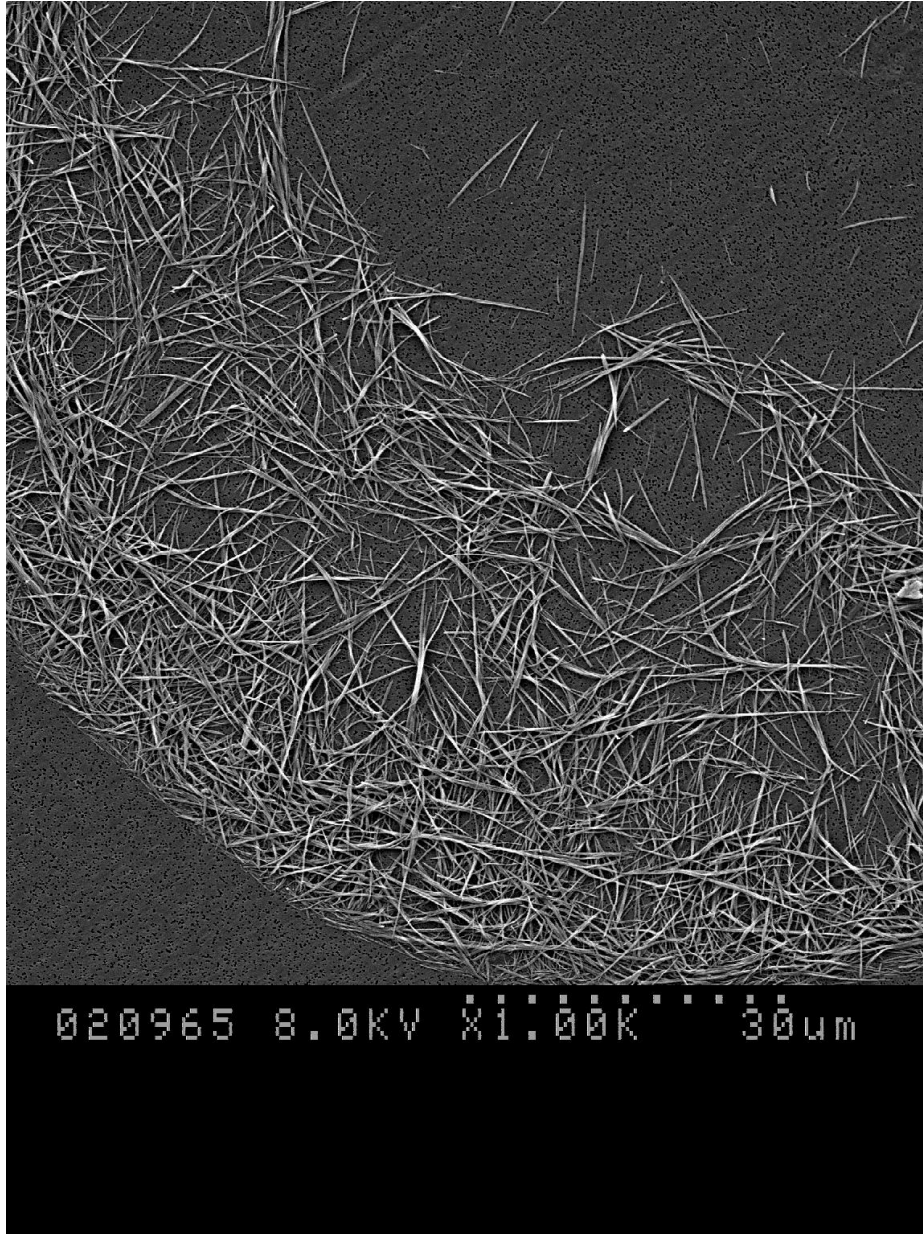


Figure 31: SEM image of particles generated with 0.5 mg/ml of CA and ambient air at 18.1 l/min at 1000x magnification

The effectiveness of the drying chamber was affected further by decreasing the flow rate. At 10.9 l/min, the droplets became larger and conjoined after landing on the polycarbonate filter. This can be seen in Figure 32. The lack of drying is likely due to the local relative humidity being extremely high as the cloud of droplets evaporates and

quickly saturates the air locally. To increase the effectiveness of the chamber, dry air was used and the pulse time was reduced to one second.

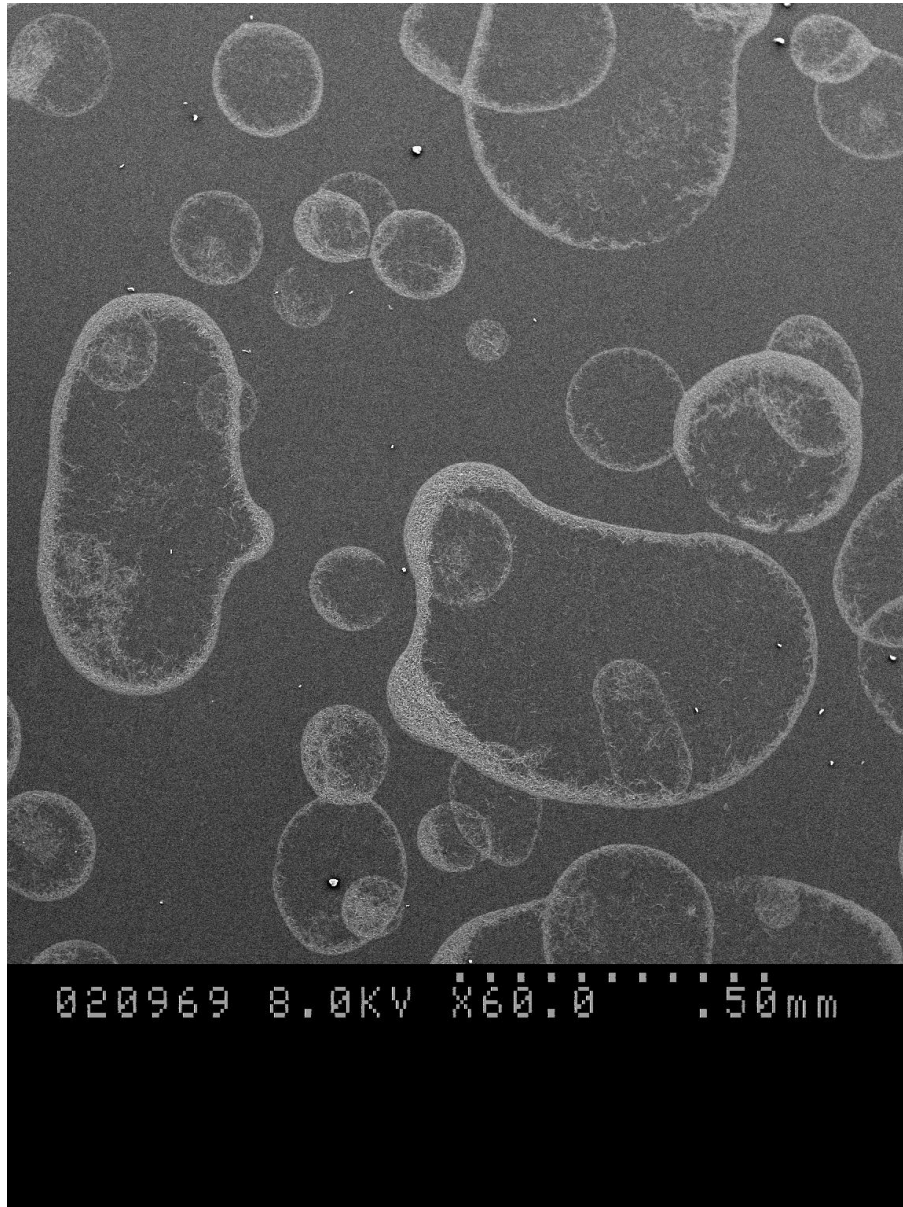


Figure 32: SEM image of particles generated with ambient air at 10.9 l/min at 60x magnification

4.3.4.2 Dry Air

Six more experiments were done with dry air at three different flow rates of approximately: 15 l/min, 7.5 l/min, and 1.0 l/min. For three of the experiments a one second pulse of 0.5 mg/ml of CA was sprayed into the chamber and the remaining three a one second pulse of 2.0 mg/ml was used. In all cases the chamber was emptied for 30 minutes. It was observed that although drying was improved (overall small droplets were seen in the images) the droplets were still not fully dried.

Some sample images are shown below for the three flow rates. Figure 33 shows a detailed image of the edge of a particle. The same structure of an increased concentration at the edge is seen. The larger, brighter particles seen in this image are dust from the environment.



Figure 33: SEM image of particles generated with dry air at 14.7 l/min at 1500x magnification

In Figure 34 a particle with a much more uniform HARP concentration is seen. This particle is smaller than those seen previously, with a diameter of approximately 50 μm . It is possible that because this particle is smaller, the drying that occurred after landing was minimal, resulting in less reduction in diameter. Also, the volume of water available to spread out onto the membrane after landing would be decreased. If this were the case, the increase in concentration at the edge would not be as prominent as that seen with larger droplets.

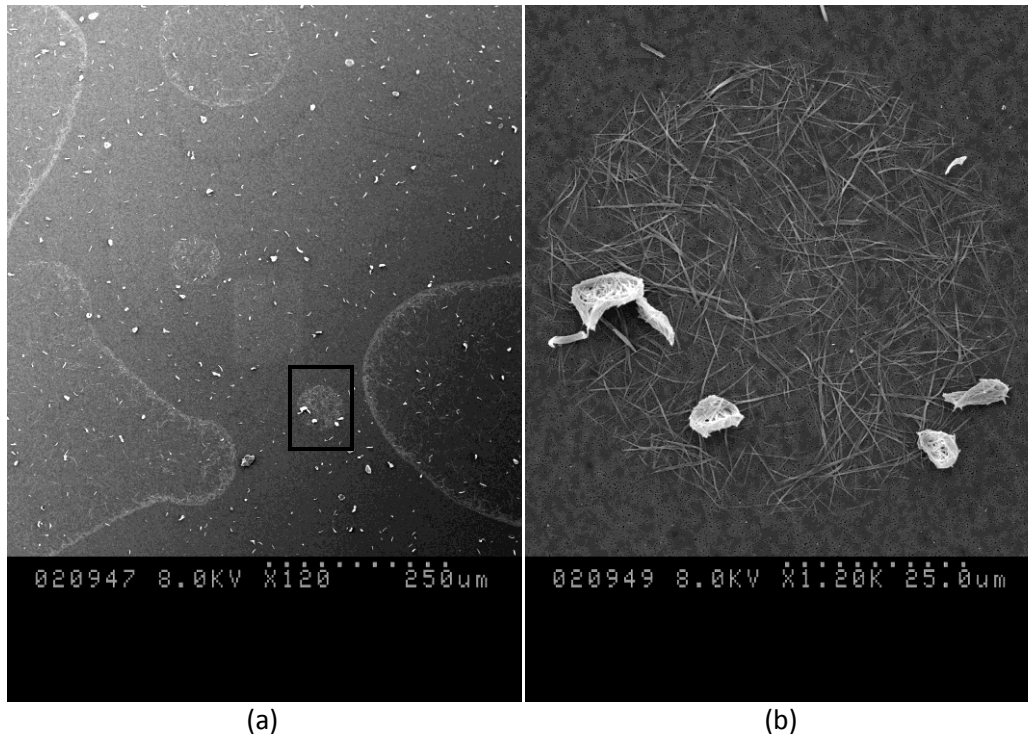


Figure 34: SEM image of particles generated with dry air at 7.4 l/min at (a) 120x magnification and (b) 1200x magnification

Figure 35 shows a larger particle from dry air at 1.0 l/min. This larger droplet shows the same structure as that found with the particles dried in the ambient air.

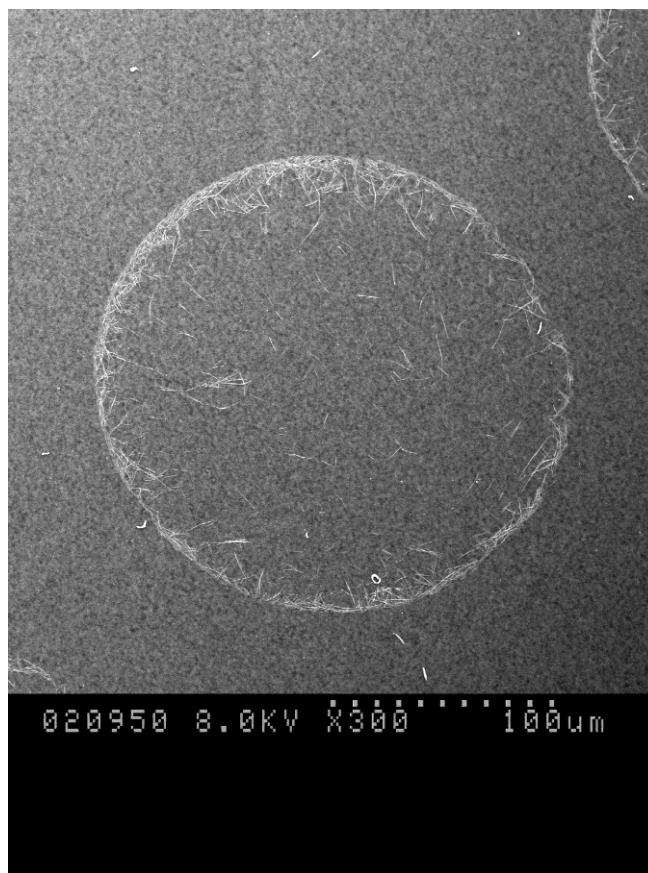
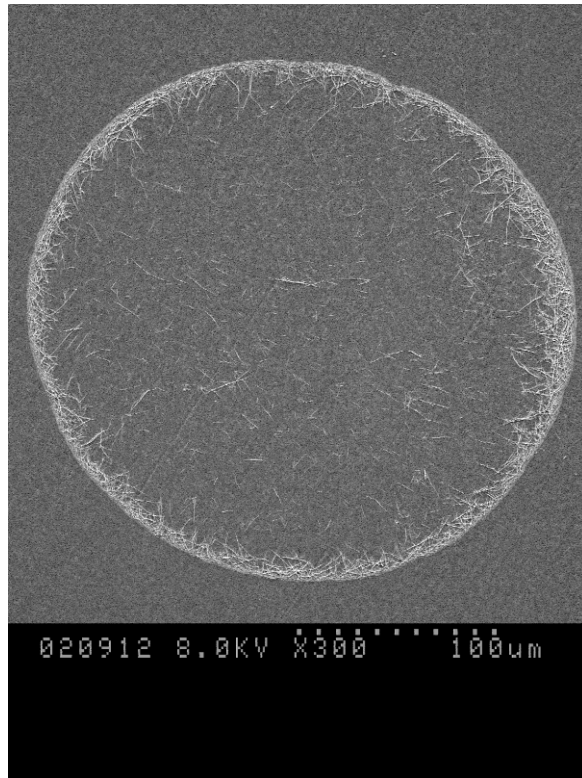
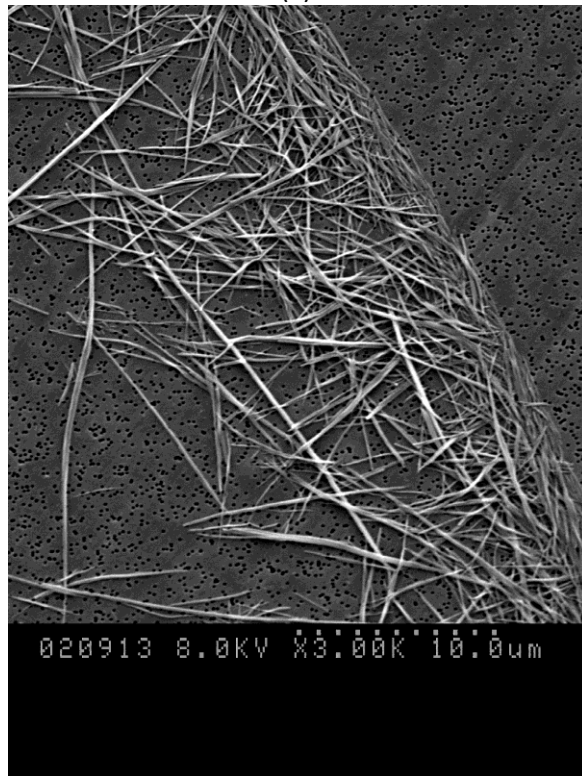


Figure 35: SEM image of particles generated with dry air at 1.0 l/min at 300x magnification

Three more samples with concentrations of 2 mg/ml were collected at flow rates of: 15.0 l/min, 7.5 l/min, and 1.0 l/min. These larger concentrations, although not desirable for the creation of individual HARPs, were used to provide more information on the structure of these shells of HARPs. As can be seen in Figure 36 the ring type formation is further emphasized at higher concentrations. Although it is likely that a shell type structure is being formed during the drying process, when the shell of HARPs lands wet this structure is lost as the droplet spreads out and flattens.



(a)



(b)

Figure 36: SEM image of CA particles of 2.0 mg/ml generated with dry air at 15.0 l/min at (a) 300x magnification and (b) 3000x magnification

When examining a smaller cluster of particles, such as that seen below in Figure 37, the distribution of HARPs is much more uniform. These smaller clusters contain much less water and are therefore more likely to retain their structure upon depositing on the polycarbonate membrane, as any remaining water would quickly evaporate.

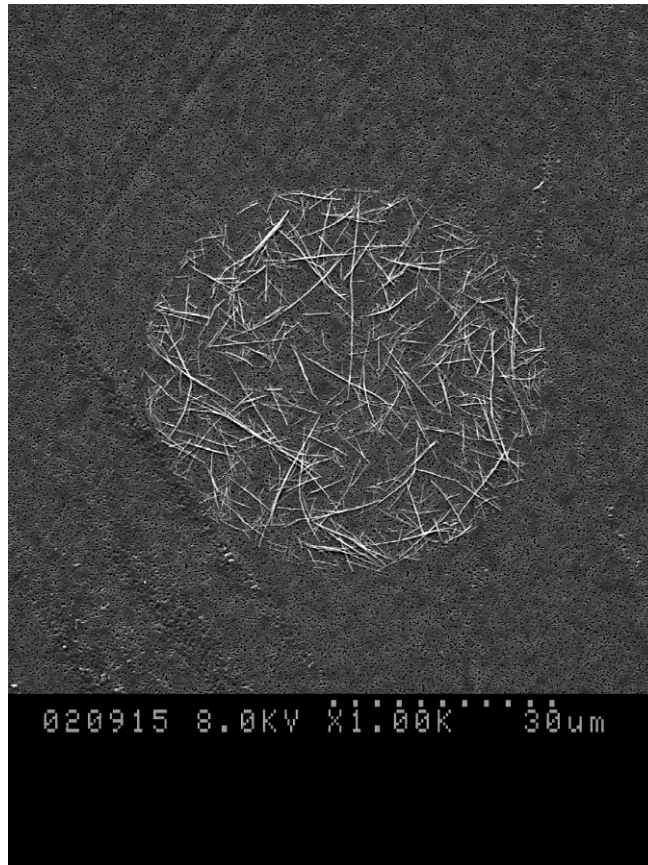


Figure 37: SEM image of CA particles of 2.0 mg/ml generated with dry air at 15.0 l/min 1000x magnification

Because this cluster of HARPs was smaller than others examined, and the structure appeared to be slightly different, the distribution of particles was examined in more detail. The cluster was separated into two areas: an inner circle with a diameter of half the total circle and the remaining outer ring. The HARPs in each of these areas were counted in order to compare the ratio of these two areas. These two areas can be

seen below in Figure 38. As discussed earlier, this ratio will aid in attempting to infer a 3D structure from the 2D SEM image.

The particles in area A and area B were counted. Where $AREA_A = \pi(r_A^2 - r_B^2)$, $AREA_B = \pi r_B^2$, and $r_B = r_A/2$ the ratio $AREA_A/AREA_B$ simplifies to 3. As concentration is our variable of interest and concentration is the particles per area in this instance, the number of particles found in A was divided by three. This was then compared to the predicted values for a uniform and shell-like particle distribution as seen in Table 8.

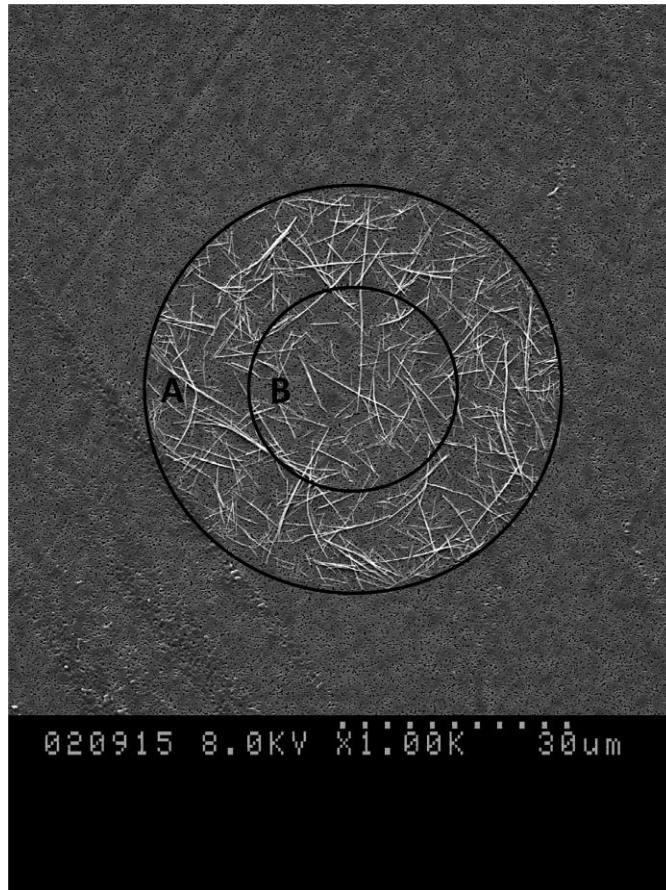


Figure 38: Division of inner and outer areas of Figure 37

Table 8: Comparison of predicted and actual particle concentrations in areas A and B

	Percentage of particles in A	Percentage of particles in B
Predicted uniform distribution	40%	60%
Predicted shell distribution	65%	35%
Figure 38 particle distribution	55%	45%

The cluster of HARPs of interest appeared to be closer to the predicted values for a shell like structure. It is likely that this was a shell-like structure with some HARPs remaining in the centre. As each droplet would start out with a uniform distribution and then develop into a shell like structure through the drying process, it is probable this particle was not fully dried, but was in the midst of forming a shell-like structure.

4.3.4.3 Orifice

The orifice was used to help aid in deaggregating the clusters of HARPs, and to improve drying by creating smaller droplets from the larger droplets entering the orifice. Clusters of particles were collected at 16 l/min on a 0.2 μm polycarbonate membrane after passing through one of three 1 mm orifices. Much smaller clusters were created, and can be seen below in Figure 39, Figure 40, Figure 41, and Figure 42. The clusters in these images range from approximately 5 to 15 μm . This corresponds to the predicted size of 7 μm of the Kolmogorov length scales. These particles are also more tightly packed together. Because of the turbulence inside the orifice, the larger undried clusters of HARPs are torn apart into these smaller clusters. With the size of these clusters now approximately an order of magnitude smaller, they are able to fully dry. Although the addition of the orifice improved the drying and created smaller clusters, the goal of creating individual HARPs was still not achieved. One possibility to further

improve this process would be to put multiple orifices in series, breaking up the clusters into smaller and smaller aggregates. However, this would likely break the HARPs and result in lengths similar to those produced previously [10].

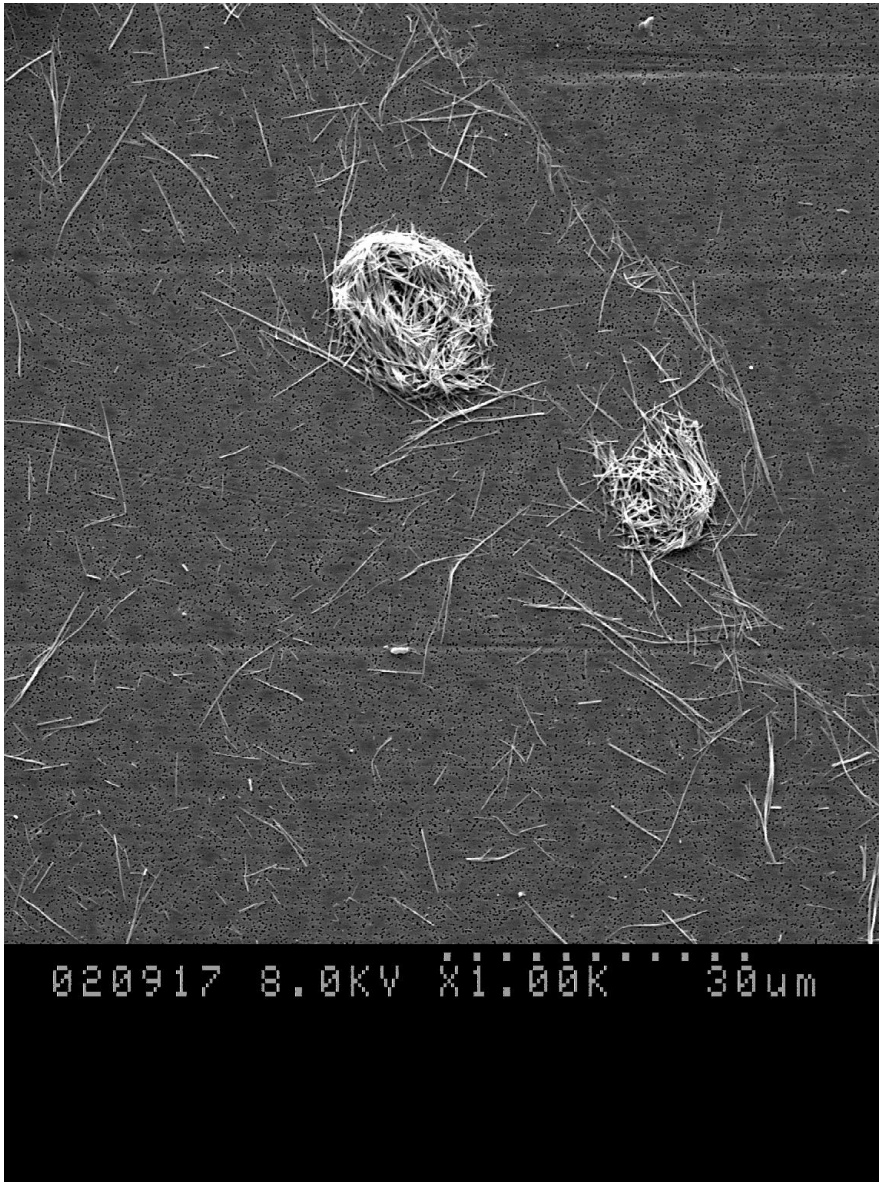
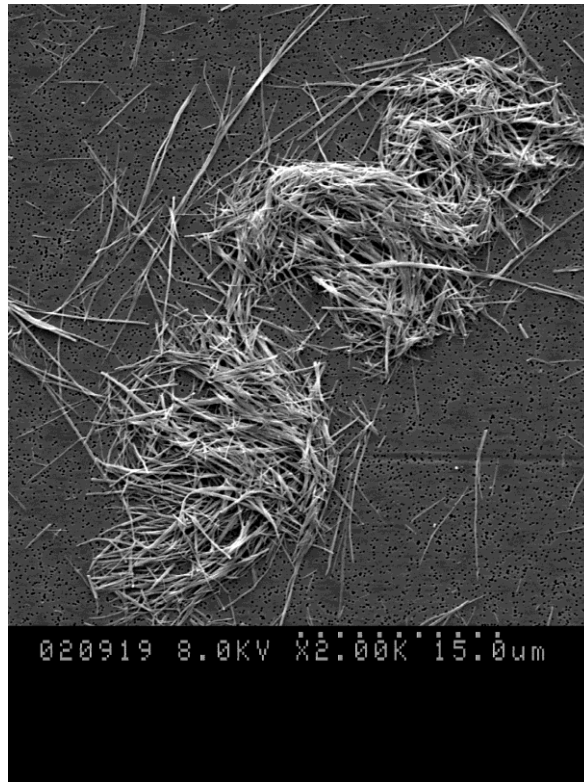
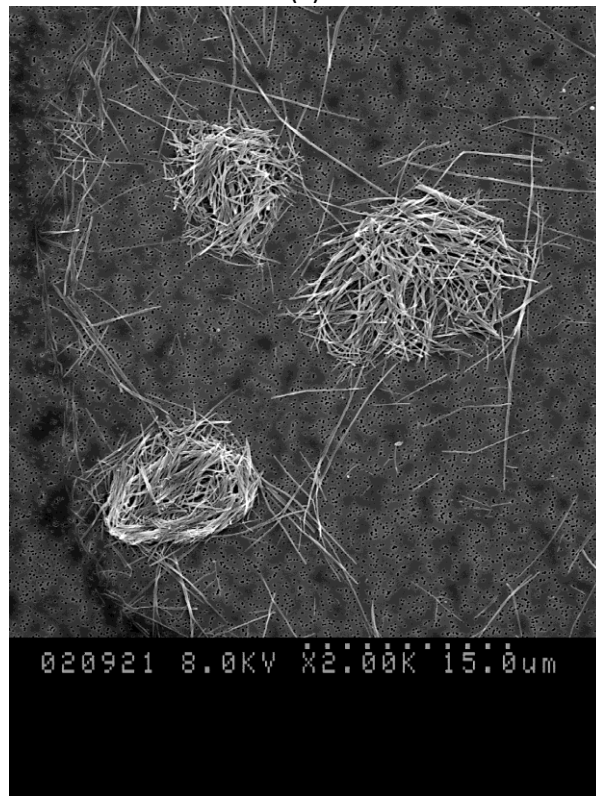


Figure 39: SEM image of CA particles of 0.5 mg/ml generated with dry air passed through an orifice at 16.0 l/min at 1000x magnification



(a)



(b)

Figure 40: SEM images of CA particles of 0.5 mg/ml generated with dry air passed through an orifice at 16.0 l/min at 2000x magnification

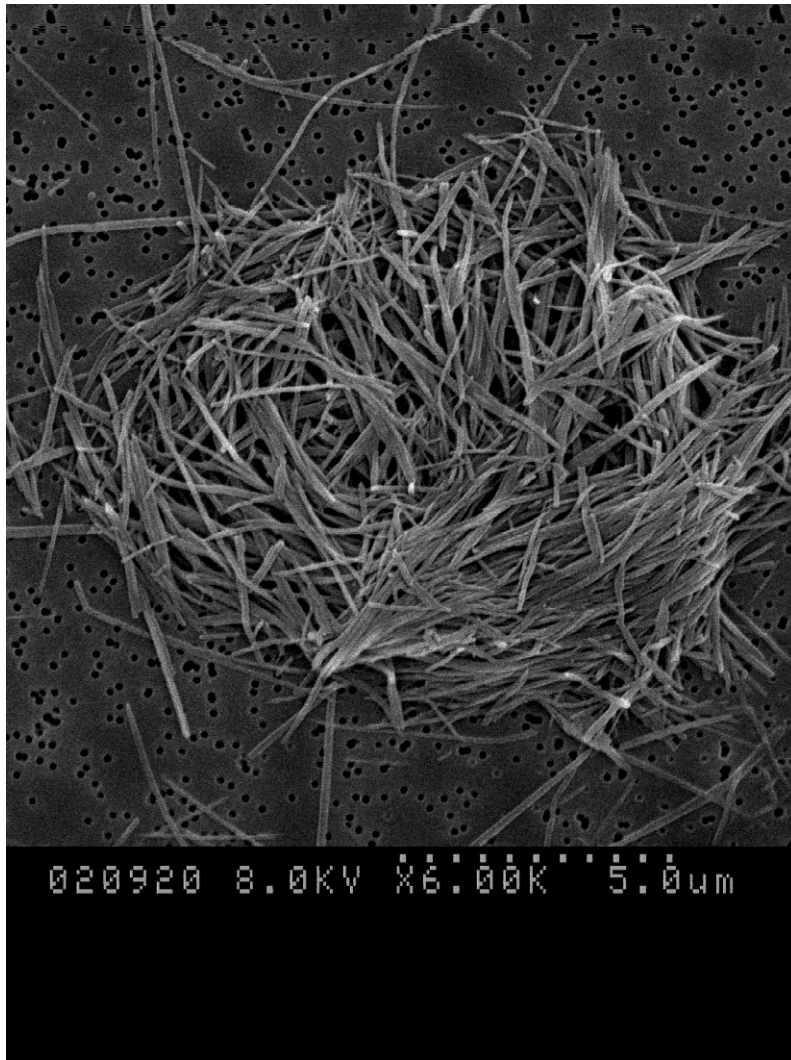


Figure 41: SEM image of CA particles of 0.5 mg/ml generated with dry air passed through an orifice at 16.0 l/min at 6000x magnification

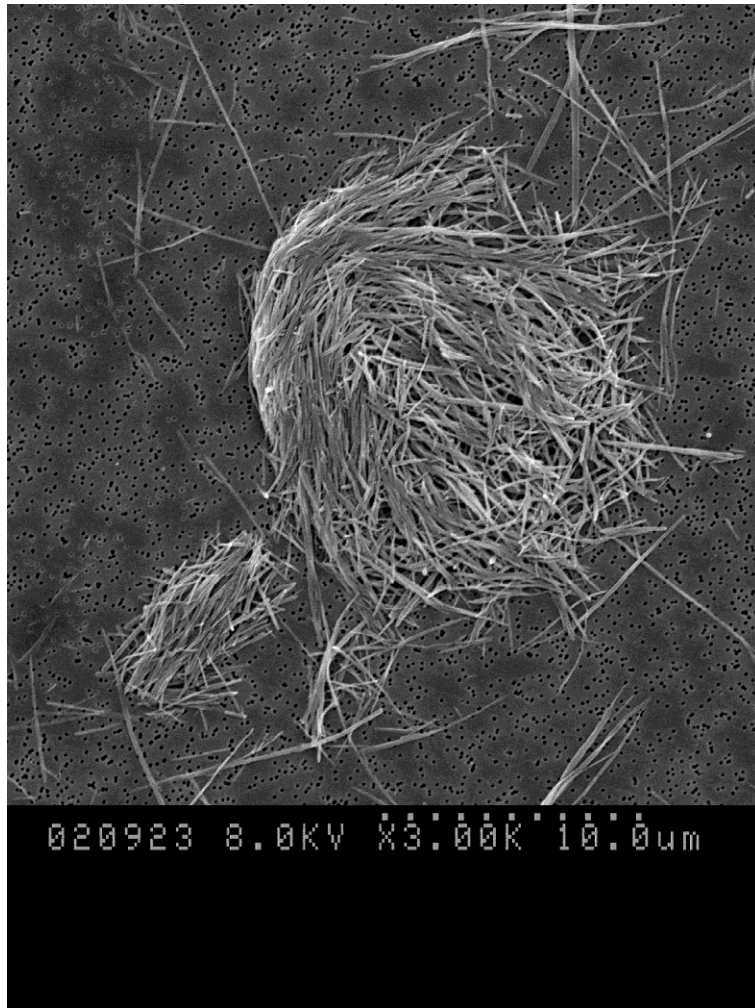


Figure 42: SEM image of two CA particles of 0.5 mg/ml generated with dry air passed through an orifice at 16.0 l/min at 3000x magnification

Although many of clusters resulting from the orifice appeared to be pieces of larger clusters that had been ripped apart, there were also some clusters which avoided being ripped apart but still experienced improved drying. One of these particles can be seen below in Figure 43.

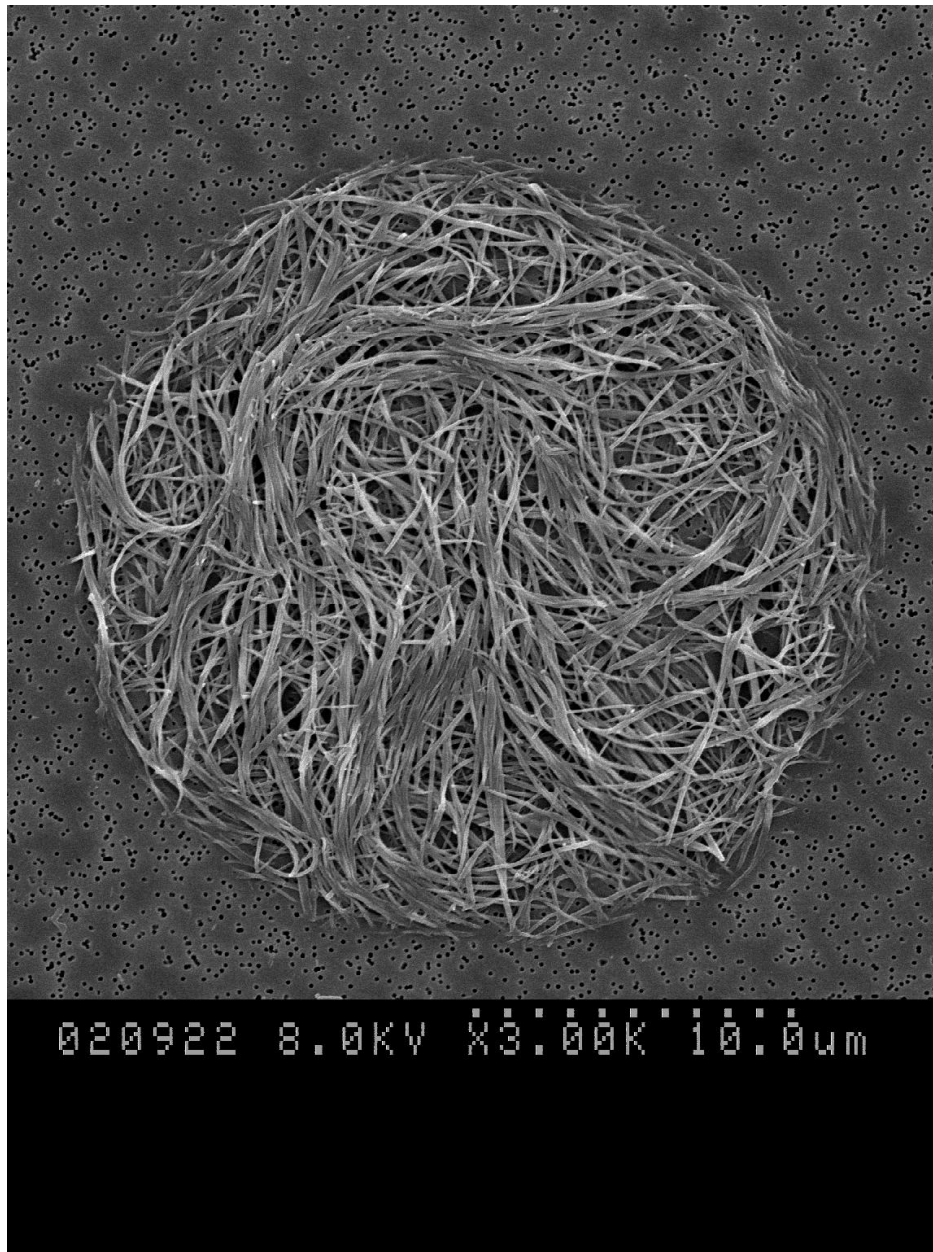


Figure 43: SEM image of CA particles of 0.5 mg/ml generated with dry air passed through an orifice at 16.0 l/min at 3000x magnification

The use of the orifice successfully achieved drying and smaller clusters. However, due to the shape of these clusters, they would not work for targeting drug delivery through controlling their orientation. Without a high aspect ratio, there is no preferred axis of magnetization, and interception is no longer the dominant mechanism of deposition.

Although these clusters were not the desired outcome of this study, their porous nature does present other advantages.

Porous particles allow larger sized particles to reach deeper regions in the lung [16]. Because of the larger size of these particles they can avoid being consumed by macrophages [16]. This lack of clearance allows more time for the particle to deliver its therapeutic agent, increasing the efficacy of the drug [16].

4.4 Conclusions

Through the use of an ultrasonic nozzle, longer HARPs were created. These HARPs had a CML of $5.9 \pm 4.2 \mu\text{m}$ with particles as long as $23 \mu\text{m}$ found. These HARPs had a much higher aspect ratio of 59. However, mainly due to restrictions on concentration, individual HARPs were not able to be created. Instead, clusters of HARPs with shell-like structures were created. Additionally, except in the case of the orifice, the droplets were not successfully dried due mainly to the local relative humidity around the droplets being very high.

5 Suggestions for Future Work

Although the results of the *in vivo* study were not statistically significant, they were trending towards significance. By refining the experiment to control additional elements of the experiment, it is hoped that statistically significant results can be controlled. Firstly, by obtaining individual $T_{1,0}$ relaxation times for each individual subject the variability in this value between the different subjects can be eliminated. Secondly, a more accurate way of segregating the lung into separate regions would provide much more detailed image of the regional deposition of the particles within the lung. With these changes in place, there will be much more confidence in the data obtained from the experiments.

From the results of the feasibility analysis, it was found that although longer HARPs were created, there were multiple HARPs together in clusters. With the complications regarding the solubility of CA and drying these larger droplets, the method outlined in this thesis is not a viable option to create individual longer HARPs. However, the predicted benefits of creating longer HARPs are still valid and a different delivery system could be designed to optimize this method of drug delivery.

Overall, the benefits of creating a targeted drug delivery system for inhaled chemotherapy warrants further research into developing and optimizing this method.

References

- [1] W.H. Finlay, *The Mechanics of Inhaled Pharmaceutical Aerosols: An Introduction*, London, UK: Academic Press, 2001.
- [2] J.S. Patton and P.R. Byron, "Inhaling medicines: delivering drugs to the body through the lungs," *Nature reviews. Drug discovery*, vol. 6, Jan. 2007, pp. 67-74.
- [3] T. Tatsumura, S. Koyama, M. Tsujimoto, M. Kitagawa, and S. Kagamimori, "Further study of nebulisation chemotherapy, a new chemotherapeutic method in the treatment of lung carcinomas: fundamental and clinical.," *British journal of cancer*, vol. 68, Dec. 1993, pp. 1146-9.
- [4] S. Sharma, D. White, a R. Imondi, M.E. Placke, D.M. Vail, and M.G. Kris, "Development of inhalational agents for oncologic use.," *Journal of clinical oncology : official journal of the American Society of Clinical Oncology*, vol. 19, Mar. 2001, pp. 1839-47.
- [5] G.A. Otterson, M.A. Villalona-Calero, S. Sharma, M.G. Kris, A. Imondi, M. Gerber, D.A. White, M.J. Ratain, J.H. Schiller, A. Sandler, M. Kraut, S. Mani, and J.R. Murren, "Phase I study of inhaled Doxorubicin for patients with metastatic tumors to the lungs.," *Clinical cancer research : an official journal of the American Association for Cancer Research*, vol. 13, Feb. 2007, pp. 1246-52.
- [6] Canadian Cancer Society/National Cancer Institute of Canada, *Canadian Cancer Statistics*, Toronto: 2010.
- [7] P. Dames, B. Gleich, A. Flemmer, K. Hajek, N. Seidl, F. Wiekhorst, D. Eberbeck, I. Bittmann, C. Bergemann, T. Weyh, L. Trahms, J. Rosenecker, and C. Rudolph, "Targeted delivery of magnetic aerosol droplets to the lung.," *Nature nanotechnology*, vol. 2, Aug. 2007, pp. 495-9.
- [8] B. Gleich, N. Hellwig, H. Bridell, R. Jurgons, C. Seliger, C. Alexiou, B. Wolf, and T. Weyh, "Design and Evaluation of Magnetic Fields for Nanoparticle Drug Targeting in Cancer," *IEEE Transactions On Nanotechnology*, vol. 6, Mar. 2007, pp. 164-170.
- [9] A.R. Martin and W.H. Finlay, "Alignment of Magnetite-Loaded High Aspect Ratio Aerosol Drug Particles with Magnetic Fields," *Aerosol Science and Technology*, vol. 42, Apr. 2008, pp. 295-298.

- [10] A. Martin and W. Finlay, "Enhanced deposition of high aspect ratio aerosols in small airway bifurcations using magnetic field alignment," *Journal of Aerosol Science*, vol. 39, Aug. 2008, pp. 679-690.
- [11] A.R. Martin and W.H. Finlay, "Magnetic Alignment of Aerosol Particles for Targeted Pulmonary Drug Delivery: Comparison of Magnetic and Aerodynamic Torques," *Journal of Computational and Theoretical Nanoscience*, vol. 5, 2008, pp. 1-4.
- [12] M.-F. Bellin, "MR contrast agents, the old and the new," *European journal of radiology*, vol. 60, Dec. 2006, pp. 314-23.
- [13] A.R. Martin, R.B. Thompson, and W.H. Finlay, "MRI measurement of regional lung deposition in mice exposed nose-only to nebulized superparamagnetic iron oxide nanoparticles.," *Journal of aerosol medicine and pulmonary drug delivery*, vol. 21, Dec. 2008, pp. 335-42.
- [14] E.R. Weibel, "What makes a good lung?," *Swiss medical weekly : official journal of the Swiss Society of Infectious Diseases, the Swiss Society of Internal Medicine, the Swiss Society of Pneumology*, vol. 139, Jul. 2009, pp. 375-86.
- [15] *The Lung: Scientific Foundations; Volume I*, New York: Raven Press, Ltd., 1991.
- [16] D.A. Edwards, J. Hanes, G. Caponetti, J. Hrkach, A. Ben-Jebria, M.L. Eskew, J. Mintzes, D. Deaver, H. Lotan, and R. Langer, "Large Porous Particles for Pulmonary Drug Delivery," *Science*, vol. 276, Jun. 1997, pp. 1868-1872.
- [17] C.G. Phillips and S.R. Kaye, "On the asymmetry of bifurcations in the bronchial tree," *Respiration physiology*, vol. 107, Jan. 1997, pp. 85-98.
- [18] E.R. Weibel and D.M. Gomez, "Architecture of the human lung. Use of quantitative methods establishes fundamental relations between size and number of lung structures.," *Science (New York, N.Y.)*, vol. 137, Aug. 1962, pp. 577-85.
- [19] W.H. Finlay, C.F. Lange, M. King, and D.P. Speert, "Lung delivery of aerosolized dextran.," *American journal of respiratory and critical care medicine*, vol. 161, Jan. 2000, pp. 91-7.
- [20] C. Crowe, M. Sommerfeld, and Y. Tsuji, *Multiphase flows with droplets and particles*, Boca Raton: CRC Press, 1998.
- [21] G.G. Stokes, "No Title," *Trans. Cambridge Phil. Soc.*, vol. 9, 1851, p. 8.

- [22] W.C. Hinds, *Aerosol Technology: Properties, behaviour, and measurement of airborne particles*, New York: John Wiley & Sons, Inc., 1999.
- [23] W. Stahlhofen, G. Rudolf, and A.C. James, "Intercomparison of Experimental Regional Aerosol Deposition Data," vol. 2, 1989.
- [24] V. Timbrell, "The Inhalation of Fibrous Dusts," *Annals of the New York Academy of Sciences*, vol. 132, 1965, pp. 255-273.
- [25] S.F. Platek, D.H. Groth, C.E. Ulrich, L.E. Stettler, M.S. Finnell, and M. Stoll, "Chronic inhalation of short asbestos fibers," *Fundamental and applied toxicology : official journal of the Society of Toxicology*, vol. 5, Apr. 1985, pp. 327-40.
- [26] G.B. Jeffery, "The Motion of Ellipsoidal Particles Immersed in a Viscous Fluid," *Proceedings of the Royal Society of London*, vol. 102, 1922, pp. 161-179.
- [27] T. Myojo, "Deposition of fibrous aerosol in model bifurcating tubes," *Journal of Aerosol Science*, vol. 18, Jun. 1987, pp. 337-347.
- [28] T. Myojo and M. Takaya, "Estimation of fibrous aerosol deposition in upper bronchi based on experimental data with model bifurcation," *Industrial health*, vol. 39, Apr. 2001, pp. 141-9.
- [29] W.D. Bennett, "Human Variation in Spontaneous Breathing Deposition Fraction: A Review," *J. Aerosol Med.*, vol. 1, 1988, pp. 67-80.
- [30] J.S. Patton, C.S. Fishburn, and J.G. Weers, "The lungs as a portal of entry for systemic drug delivery," *Proceedings of the American Thoracic Society*, vol. 1, Jan. 2004, pp. 338-44.
- [31] N.R. Labiris and M.B. Dolovich, "Pulmonary drug delivery. Part I: Physiological factors affecting therapeutic effectiveness of aerosolized medications," *British Journal of Clinical Pharmacology*, vol. 56, Dec. 2003, pp. 588-599.
- [32] S.H. Curry, A.J. Taylor, S. Evans, S. Godfrey, and E. Zeidifard, "Disposition of Disodium Cromoglycate Administered in Three Particle Sizes," *Br. J. clin. Pharmac.*, vol. 2, 1975, pp. 267-270.
- [33] J. Rosenstock, J.C. Cappelleri, B. Bolinder, and R. a Gerber, "Patient satisfaction and glycemic control after 1 year with inhaled insulin (Exubera) in patients with type 1 or type 2 diabetes.," *Diabetes care*, vol. 27, Jun. 2004, pp. 1318-23.

- [34] Y. Geng, P. Dalhaimer, S. Cai, R. Tsai, M. Tewari, T. Minko, and D.E. Discher, "Shape effects of filaments versus spherical particles in flow and drug delivery.," *Nature nanotechnology*, vol. 2, Apr. 2007, pp. 249-55.
- [35] P. Camner, M. Anderson, K. Philipson, A. Bailey, A. Hashish, N. Jarvis, M. Bailey, and M. Svartengren, "Human Bronchiolar Deposition and Retention of 6-, 8-, and 10- μm Particles," *Experimental Lung Research*, vol. 23, Jan. 1997, pp. 517-535.
- [36] K. Selting, J.C. Waldrep, C. Reiner, K. Branson, D. Gustafson, D.Y. Kim, C. Henry, N. Owen, R. Madsen, and R. Dhand, "Feasibility and safety of targeted cisplatin delivery to a select lung lobe in dogs via the AeroProbe intracorporeal nebulization catheter.," *Journal of aerosol medicine and pulmonary drug delivery*, vol. 21, Sep. 2008, pp. 255-68.
- [37] I. Balashazy, T.B. Martonen, and W. Hofmann, "Fiber Deposition in Airway Bifurcations," *Journal of Aerosol Medicine*, vol. 3, Jan. 1990, pp. 243-260.
- [38] R.F. Phalen, M.J. Oldham, and R.K. Wolff, "The relevance of animal models for aerosol studies," *Journal of aerosol medicine and pulmonary drug delivery*, vol. 21, Mar. 2008, pp. 113-24.
- [39] H.-K. Chan and I. Gonda, "Aerodynamic properties of elongated particles of cromoglycic acid," *Journal of Aerosol Science*, vol. 20, 1989, pp. 157-168.
- [40] T. Suwa, S. Ozawa, M. Ueda, N. Ando, and M. Kitajima, "Magnetic resonance imaging of esophageal squamous cell carcinoma using magnetite particles coated with anti-epidermal growth factor receptor antibody.," *International journal of cancer. Journal international du cancer*, vol. 75, Feb. 1998, pp. 626-34.
- [41] S. Rosenthal, H. Willich, W. Ebert, and J. Conrad, "The demonstration of human tumors on nude mice using gadolinium-labeled monoclonal antibodies for magnetic resonance imaging," *Invest. Radiol.*, vol. 28, 1993, pp. 789-793.
- [42] R.B. Schlesinger and L.A. McFadden, "Comparative morphometry of the upper bronchial tree in six mammalian species.," *The Anatomical record*, vol. 199, Jan. 1981, pp. 99-108.
- [43] F.J. Miller, R.R. Mercer, and J.D. Crapo, "Lower Respiratory Tract Structure of Laboratory Animals and Humans: Dosimetry Implications," *Aerosol Science and Technology*, vol. 18, 1993, pp. 257-271.

- [44] J.D. Schroeter, J.S. Fleming, D. Hwang, and T.B. Martonen, "A computer model of lung morphology to analyze SPECT images.," *Computerized medical imaging and graphics : the official journal of the Computerized Medical Imaging Society*, vol. 26, 2002, pp. 237-46.
- [45] A.R. Martin, "Enhanced Airway Deposition of High Aspect Ratio Pharmaceutical Aerosols through Magnetic Field Alignment for Localized Targeting within the Lung," 2008.
- [46] S.L. Katz, S.L. Ho, and A.L. Coates, "Nebulizer choice for inhaled colistin treatment in cystic fibrosis," *CHEST*, vol. 119, Jan. 2001, pp. 250-5.
- [47] Sono-tek Corporation, "Ultrasonic Atomizing Nozzle Systems: Operating Instructions," 2009.
- [48] Y.A. Cengel and M.B. Boles, *Thermodynamics: An Engineering Approach, Fourth Edition*, 2002.
- [49] D.S. Wishart, C. Knox, A.C. Guo, D. Cheng, S. Shrivastava, D. Tzur, B. Gautam, and M. Hassanali, "DrugBank: a knowledgebase for drugs, drug actions and drug targets.," *Nucleic acids research*, vol. 36, Jan. 2008, pp. D901-6.
- [50] H. Tennekes and J.L. Lumley, *A First Course in Turbulence*, Cambridge, MA: MIT Press, 1972.
- [51] F.M. White, *Viscous Fluid Flow*, New York: McGraw-Hill, 1991.
- [52] S.F. Platek, R.D. Riley, and S.D. Simon, "The classification of asbestos fibres by scanning electron microscopy and computer-digitizing tablet.," *The Annals of occupational hygiene*, vol. 36, Apr. 1992, pp. 155-71.
- [53] R. Vehring, "Pharmaceutical particle engineering via spray drying.," *Pharmaceutical research*, vol. 25, May. 2008, pp. 999-1022.
- [54] E.H.-J. Kim, X. Dong Chen, and D. Pearce, "On the Mechanisms of Surface Formation and the Surface Compositions of Industrial Milk Powders," *Drying Technology*, vol. 21, Mar. 2003, pp. 265-278.
- [55] N. Tsapis, D. Bennett, B. Jackson, D.A. Weitz, and D.A. Edwards, "Trojan particles: large porous carriers of nanoparticles for drug delivery.," *Proceedings of the National Academy of Sciences of the United States of America*, vol. 99, Sep. 2002, pp. 12001-12005.
- [56] B. Asgharian, C.P. Yu, and L. Gradon, "Diffusion of Fibers in a Tubular Flow," *Aerosol Science and Technology*, vol. 9, 1988, pp. 213-219.

- [57] F. Sabbadin, M. Turatto, R. Ragazzoni, E. Cappellaro, and S. Benetti, “The structure of planetary nebulae : theory vs . practice,” *Astronomy*, vol. 949, 2006, pp. 937-949.